From gondwana rifting to alpine orogeny

Ali Mohammadi, Jonas Ruh, Marcel Guillong, Oscar Laurent, Lotfollah Aghajari

FROM GONDWANA RIFTING TO ALPINE OROGENY: DETRITAL ZIRCON GEOCHRONOLOGIC AND PROVENANCE SIGNALS FROM THE KOPET DAGH BASIN (NE IRAN)

ALI MOHAMMADI*,†, JONAS B. RUH**, MARCEL GUILLONG**, OSCAR LAURENT**,***, and LOTFOLLAH AGHAJARI§

* Eurasia Institute of Earth Sciences, Istanbul Technical University, Maslak, Istanbul, Turkey

** Department of Earth Sciences, ETH Zürich, Sonneggstrasse 5, 8092 Zürich, Switzerland

*** CNRS, Géosciences Environnement Toulouse, Observatoire Midi-Pyrénées, 14 avenue Edouard Belin F-31400 Toulouse, France

§ Exploration Directorate, National Iranian Oil Company, Sheikh Baha'i Square, Seoul Street, Tehran, Iran

ABSTRACT. The Kopet Dagh mountains in NE Iran exhibit a 7-km-thick continuous sedimentary sequence recording detritus from exposed surrounding terranes from the last 175 Myr. This work presents a multi-disciplinary geochronologic and provenance analysis in an attempt to identify and date major geologic events along the northern segment of the Tethys and reconstruct the regional tectonic history from Gondwana-related rifting until Alpine orogeny. Sandstone framework, heavy mineral analysis, U-Pb dating of detrital zircons, and Hf-isotope ratio measurements on dated zircons from Triassic to Paleocene sandstones indicate three main tectonic events that include early Silurian intracontinental rifting (opening of Paleo-Tethys), early Carboniferous rifting of a back-arc basin (Aghdarband Basin), and Late Triassic collisional to post-collisional magmatism(Paleo-Tethys collision). Mineralogical and age peak considerations indicate that detritus was supplied from the south into the extensional Kopet Dagh Basin during Middle Jurassic, while Cretaceous to Paleocene sandstones show signs of increasing cannibalism.

Keywords: Gondwana, Kopet Dagh Basin, Paleo-Tethys, Neo-Tethys, Rifting, Collision, Detrital zircon, Hf isotopes, Provenance anlysis

INTRODUCTION

The long-standing tectonic history between Gondwana and Eurasia includes several phases of rifting and collision, recorded by magmatic and metamorphic episodes in various domains of related orogenic belts; from the Alps in the west to the Himalayas in the east (for example

Şengör, 1990a; 1990b; Stampfli, 2000; Stampfli and Borel, 2002). The timing of main tectonic episodes including rifting, subduction initiation, and collision are crucial for the reconstruction of plate tectonics (for example Stampfli and Borel, 2002). Geochronology and geochemistry of magmatic and metamorphic rocks are widely applied in geodynamic studies to constrain the timing and other characteristics of tectonic events (for example Barbarin, 1999; Brown, 2014). However, the occurrence and surface exposure of such igneous and metamorphic terranes may be limited in some tectono-sedimentary domains because of complete erosion or coverage by younger sediments. In addition, the application of different dating methods on igneous and metamorphic rocks provides a wide range of ages, which makes the exact timing of tectonic events difficult. In fact, timing constraints for tectonic events based only on magmatic or metamorphic rocks may be misleading. A more accurate detection of large-scale tectonic events can be found in clastic sedimentary successions, where the detritus source rapidly responds to any plate tectonic reorganization (Cawood and others, 2012; Fedo and others, 2003). Therefore, provenance analysis, zircon geochronology, and zircon isotopic composition on detrital sandstones may help to improve the precision when constraining the timing of tectonic events (for example Cawood and others, 2012; Weltje and von Eynatten, 2004).

Several episodes of continental rifting and collision took place between Gondwana and Eurasia since the Palaeozoic until the Cenozoic that ultimately climaxed in the Alpine-Himalayan orogeny (for example Şengör and others, 1984; Stampfli, 2000; Stampfli and Borel, 2002; Stöcklin, 1974). Separation of several continental slivers and microcontinental blocks from Gondwana occurred in two phases, coeval with the opening of two ocean basins, the Paleo-Tethys and Neo-Tethys oceans (for example Alavi, 1996; Stampfli, 2000; Şengör and others, 1984; Stöcklin, 1974). The opening of the Iranian segment of the Paleo-Tethys between the Iranian continent (Gondwana) and the Turan platform (Eurasia) was suggested to have occurred in the Early Palaeozoic (Ordovician-Silurian) based on ages of oceanic basalts (Boulin, 1988; Stampfli, 2000). The subsequent northwards subduction of the Paleo-Tethys beneath Eurasia

initiated during the Late Devonian and continued until the Late Triassic as shown from dating of the Darrehanjir–Mashhad ophiolites (for example Moghadam and others, 2015a; Stampfli, 2000; Wilmsen and others, 2009). The opening of a new ocean (Neo-Tethys Ocean) between the Arabian plate and the Central Iran block at the end of the Permian went hand in hand with the northward movement of the Central Iran block, resulting in the closure of the Paleo-Tethys Ocean in the Late Triassic, and the consequent collision of the Iranian plate with the Turan block; the Cimmerian orogeny (for example Berberian and King, 1981; Muttoni and others, 2009; Şengör, 1979; Zanchetta and others, 2013). This Cimmerian orogeny prevented further shortening along the northern segment of the Tethys and triggered the onset of subduction of the southern Neo-Tethys Ocean (for example Zanchetta and others, 2013).

The northward subduction of the Neo-Tethys Ocean beneath the Central Iran block was accompanied by the opening of the Greater Caucasus–South Caspian–Kopet Dagh basins during the Middle Mesozoic, potentially in form of a larger back-arc basin (Alavi et al, 1997; Brunet and Cloetingh, 2003; Zanchi and others, 2006). The Neo-Tethys Ocean finally closed during the collision of the Arabian plate and Central Iran block in late Oligocene, which resulted in the Alpine orogeny (Pirouz and others, 2017). This collision related to the closure of the Neo-Tethys resulted in tectonic inversion of previously extensional domains (Greater Caucasus, South Caspian, and Kopet Dagh basins) along the Paleo-Tethys suture (for example Robert and others, 2014; Ruh and Vergés, 2018; Ruh, 2019).

The Kopet Dagh Basin contains a stratigraphic record covering the last ~175 Myr (Middle Jurassic to Neogene sedimentary succession; Afshar Harb, 1982a; Moussavi-Harami and Brenner, 1990). Detailed provenance analysis of this shallowing-upward (deep marine–marine–deltaic–continental) sequence allows i) to reconstruct the Mesozoic-Tertiary sedimentary evolution of the Kopet Dagh Basin, ii) to clarify the general tectonic setting associated with the Turan and Iran plates, and finally iii) to precisely constrain the timing of rifting and collision events related to the opening and closure of the Paleo-Tethys and Neo-Tethys oceans.

In this study, we present combined results from sandstone modal framework, heavy mineral assemblage analysis, detrital zircon U-Pb age, and *in-situ* Hf isotope composition of Triassic (pre-rift basement), and Middle Jurassic to Paleocene detrital sediments from the Kopet Dagh. Results are interpreted to identify and characterize the respective source rocks in terms of ages and genesis. Based on these data, we determine the provenance of sedimentary detritus and reconstruct the variety of rift-related, continental arc, and post-collisional tectonic settings from Gondwana-related rifting (opening of Paleo-Tethys) to Alpine orogeny (closure of Neo-Tethys).

GOLOGY OF THE KOPET DAGH

Tectonic Setting

The Kopet Dagh mountains in NE Iran strike over 700 km along the Iran–Turkmenistan border and form the northern limit of the Alpine-Himalayan orogeny (Golonka, 2004: Robert and others, 2014; fig. 1). The Main Kopet Dagh Fault (MKF) and the East Alborz and Binalud mountains mark the northern and the southern boundary of the Kopet Dagh Basin, respectively (fig. 1). Tectonically, the Kopet Dagh Basin formed as an extensional back-arc to the Neo-Tethys subduction system farther to the south (Mangino and Priestley, 1998). The onset of extension is marked by a major nonconformity at the base, and rapid sediment facies and thickness variations in the Middle Jurassic (165 Ma to 170 Ma) deep-marine turbiditic sediments (Kavoosi and others, 2009; Robert and others, 2014; Thomas and others, 1999). In contrast to the Caspian Sea Basin in the west, there is no evidence for the formation of oceanic crust beneath the Kopet Dagh Basin (Brunet and others, 2003). After this rifting event, the basin experienced a phase of tectonic quiescence for at least 130 Myr until Oligocene-Miocene, when the extensional basins along the Paleo-Tethys suture experienced tectonic inversion as a consequence of the collision of Arabian and Eurasian plates to form the Zagros mountain range,

and due to newly arranged relative plate motions (Hollingsworth and others, 2010; Lyberis and Manby, 1999). This tectonic inversion is synchronous with the onset of deposition of continental sedimentary facies in the Kopet Dagh Basin (Robertand others, 2014) and tectonic uplift of the Alborz mountains (Razaeian and others, 2012). Uplift of the Kopet Dagh mountains resulted in widespread folding and faulting of the Jurassic to Tertiary stratigraphy and an estimated N-S shortening of ~75 km (Allen and others, 2003; Lyberis and Manby, 1999). The compressional phase continued for about 15 Myr, with an increased component of dextral strike-slip movement since ~10 Ma (Hollingsworth and others, 2006).

Stratigraphy

The study area is located in the eastern part of the Kopet Dagh Basin covered by the Darreh Gaz, Mashhad, Sarakhs, Torbat-e-Heydarieh, and Torbat-e-Jam 1:250,000 geological maps published by the Geological Survey of Iran (figs. 1, 2; Afshar 1982a, 1982b; Afshar and others, 1986; Behrouzi and others, 1993; Vaezi Pour and others, 1992). An up to seven-kilometers-thick terrigenous and carbonate s edimentary succession was deposited into the Kopet Dagh Basin between Middle Jurassic to Neogene (figs. 2, 3; Moussavi-Harami and Brenner, 1990). The Middle Jurassic (late Bajocian to Bathonian) intervals of deep marine turbiditic conglomerate, thin- and thick-bedded sandstones, siltstone, and mudstone (Kashafrud Formation) are the oldest sediments deposited into the Kopet Dagh Basin (for example Poursoltani and Gibling, 2011; Poursoltani, and others, 2007). The Middle Jurassic sediments rest unconformably on Triassic basic intrusions and volcanogenic sedimentary rocks and exhibit variations in thickness across major extensional basement faults, indicating a syn-rifting depositional environment (Robert and others, 2014; Thomas and others, 1999). Thickness of the turbiditic sediments vary between 280 m to over 2000 m in the East Kopet Dagh Basin (fig. 3). The Middle Jurassic turbiditic succession is unconformably overlain by Upper Jurassic (Callovian-Kimmeridgian) thick (>1200 m) marine carbonates and shallow marine, coastal

plain silisiclastic sediments (Mozduran Formation; Kavoosi and others, 2009; Lasemi, 1995; fig. 3). Thick fluvial siliciclastic sediments of the Early Cretaceous (Surijeh Formation) record epicontinental sea retogradation in the eastern part of the Kopet Dagh Basin (fig. 3; Moussavi-Harami and Brenner, 1990). Contemporaneous deposition of marine carbonate indicates the presence of a marine environment in the western Kopet Dagh Basin. Further transgression established a marine depositional environment throughout the entire Kopet Dagh Basin until Late Cretaceous (Turonian). This transgressions system is characterized by intervals of oolitic limestone (Tirgan Formation), marl and shale (Sarcheshmeh Formation), shale (Sanganeh Formation), and glauconitic-carbonatic sandstone and shale (Aitamir Formation; fig. 3). This wide range of lithologies indicates sea level fluctuation and depositional environments represented by tidal flats, lagoons, carbonate ramps, continetal shelfs, and shallow marine-shorefaces. A short-lived sea retogradation during the Late Cretaceous (Turonian) is responsible for an unconformity between the shallow marine glauconitic shale (Aitamir Formation) and shallow marine marl and limestones (Abderaz Formation; fig. 3). Between the Turonian until the Paleocene, the East Kopet Dagh Basin experienced other transgressional episodes characterized by marine environments including the deposition of shallow marine marl and limestones (Abderaz Formation), shelf and open marine marl and shale (Abtalkh Formation), shallow marine and shoreface glauconitic sandstone (Neyzar Formation), and shallow carbonate platform sandy limestones (Kalat Formation; fig. 3). Basin-scale sea retrogradation and surface exposure of strata is recorded by erosional surfaces within the uppermost part of Late Cretaceous sandy limestones (Kalat Formation; Mahboubi and others, 2006). In early Paleocene, reddish fluvial and lacustrine mudstones and sandstones (Pestehleigh Formation) were unconformably deposited onto uppermost Cretaceous marine sediments. During the late Paleocene, the Kopet Dagh Basin gradualy changed from a shallow continental sedimentary environment to a shallow carbonate paltform with marl and limestone sediments (Chehel Kaman Formation). The basin subsidence continued until Eocene-early Oligocene, when

marine shale and sandstones (Khangiran Formation) conformably overlayed late Paleocene sediments. Repeated minor phases of transgressions and regressions followed into the Miocene, until the basin was tectonically inverted duing Alpine orogeny, accompanied by deposition of continental conglomerates, sandstones, and shale (Neogene red beds; fig. 3).

METHODS

Nineteen sandstone samples including one sandstone sample of a lens within Triassic polymictic conglomerate, and eighteen well-cemented medium-grained Jurassic to Paleocene turbiditic, fluvial-deltaic, and continental sandstone samples were investigated (with prefix KD-01–20 in the ETH collection). Studied sandstones represent five different litho-stratigraphic formations (Qara-Gheitan, Kashafrud, Shurijeh, Aitamir, and Pestehleigh formations) of the Kopet Dagh Basin (figs 1, 2, 3 and table S1). We combined sandstone framework composition and heavy mineral analysis, detrital zircon U-Pb geochronology, and *in-situ* Hf-isotopic composition to reconstruct the lithological composition of the source-rocks and the tectonic evolution of the source area.

Sandstone thin section

Sandstones modal framework analysis was performed in thin sections stained for carbonates and feldspars with the Gazzi-Dickinson method (Dickson, 1966; Norman, 1974). For statistical reliability, at least 300 lithic fragments were counted in each thin section (Folk, 1980). The Zuffa method was applied to count detrital grains (Zuffa, 1985). Sand size lithic fragments (>63 µm) within rock fragments were counted as monomineralic grains. Results were converted to percentages for compositional comparison (Weltje and von Eynatten, 2004; table S2). Five standard complementary triangular diagrams were used to display the data (QFL, QmFLt, LvhLsLm, QmPK, and QpLvLsm; Folk, 1980; Dickinson, 1985).

Heavy mineral separation

Approximately 2-3 kg of fresh rock were collected at each sample site for heavy mineral analysis. To obtain transparent heavy mineral fractions, sandstones were crushed with the SelFrag apparatus batch equipment using high voltage (130-150 kV) pulse power technology, which liberates morphologically intact minerals. From the <2 mm sieved fraction, carbonate was dissolved in warm (60-70°C), 10%-acetic acid. Heavy minerals were pulled out in separation funnels (Mange and Maurer, 1992) from 63 µm to 400 µm sieve fractions using bromoform (density 2.88 g/cm^3). The bulk heavy mineral fractions were mounted in piperine (Martens, 1932) between a glass slab and a cover. Identification and quantification were carried out under a petrographic microscope by applying the mid-point ribbon and fleet counting methods. At least 200 grains were counted per sample (Mange and Maurer, 1992; table SI3).

Zircon geochronology

Zircons were extracted from additional 2-3 kg of fresh sandstones crushed with the SelFrag apparatus. Standard Holman-Wilfley shaking tables and magnetic separation methods (Frantz magnetic separator) delivered mineral fractions enriched in zircons. Zircons of grain fraction 60-250 µm (non-magnetic) were handpicked under a binocular microscope. Selected grains were mounted in U- and Pb-free resin, polished to expose the internal parts of the minerals, and coated with carbon. Suitable zircon domains and inclusions were identified by cathodoluminescence (CL) and backscattered-electron (BSE) images obtained by split screen on a CamScan CS44 Scandunk Viermalning electron microscope (SEM; Tescan a.s., Brno) at ETH Zurich, and analyzed with laser ablation inductively coupled mass spectrometry (LA-ICP-MS) at ETH Zurich with an excimer laser (ArF 193 nm). Zircon characteristics were interpreted following the approach by Corfu and others (2003).

The laser ablation ICP-MS analyses were performed with a RESOlution (Australian Scientific Instruments/Applied Spectra) laser ablation system at ETH Zurich equipped with a dual-volume

S-155 ablation cell (Laurin Technic, Australia), coupled to an Element XR (Thermo Scientific, Germany) sector-field ICP-MS. A laser repetition rate of 5 Hz, energy density of ca. 2.5 J/cm^2, and spot diameter of 30 μm were applied. The carrier gas consisted of high-purity He (ca. 0.7 L/min) and make-up Ar (ca. 1 L/min) from the ICP-MS. Data acquisition time per spot was about 1 minute (30 s gas blank + 30 s ablation). The data were processed with the Igor Pro Iolite v2.5 software (Hellstrom and others, 2008), using the VizualAge data reduction scheme (Petrus and Kamber, 2012). Laser-induced element fractionation (after Paton and others, 2010), instrumental mass discrimination, and drift through the analytical session were corrected by standard bracketing against zircon reference material "GJ-1" (using isotope ratios recommended by Horstwood and others, 2016). The quoted uncertainties for each individual analysis correspond to the internal error and propagated uncertainty based on the scatter of the primary reference material (see Paton and others, 2010). The accuracy and reproducibility within each run of analysis were monitored by periodic measurements of zircon reference materials "Plešovice" (337 Ma; Sláma and others 2008) and "91500" (1065 Ma; Wiedenbeck and others 1995). More details about the analytical conditions, the data from unknowns and reference materials are provided in table S5. Concordia diagrams were obtained using ISOPLOT v.3.0 (Ludwig, 2003). A concordant age is given by the overlap of the error ellipse with the Concordia age curve. In this study, ages with discordance >5% are not included for further interpretation (table S4). The frequency U-Pb age distribution diagram or probability density plot described by Ludwig (2003) includes a histogram representing the number of individual zircon grains within a short age range, and the probability curve depicts the mean age peaks of the contained age populations in one sample.

Zircon Lu-Hf isotopic analyses

Lu–Hf analyses were obtained by laser ablation multi-collection inductively coupled plasma mass spectrometry (LA-MC-ICP-MS) at ETH Zurich, using a RESOlution (ASI/Applied Spectra) excimer (ArF) 193 nm laser ablation system attached to Nu Plasma II (Nu Instruments)

multi-collector ICP-MS. A laser repetition rate of 5 Hz, a spot diameter of 50 μm, and a laser energy density of ca. 4 J/cm^2 was applied. Ablation was performed in a dual-volume, fast-washout S-155 ablation cell (Laurin Technic) fluxed with carrier gas consisting of ca. 0.37 L/min He and make-up gas consisting of ca. 0.92 L/min Ar. A typical run consisted of 40 s of background measurement followed by 40 s of sample ablation with an integration time of 0.5 s. The ICP-MS instrument was optimized for maximum sensitivity on ^{180}Hf, and optimal peak shape and coincidence for Yb, Lu, and Hf isotopes. The list of acquired masses and corresponding Faraday cups are provided in table S7.

The resulting intensities were processed offline with the Igor Pro Iolite v2.5 software, using an in-house data reduction scheme (Hellstrom and others, 2008). Background-subtracted intensities were used to calculate isotope ratios, which were corrected for instrumental mass bias by normalization to the natural abundance ratios ^{173}Yb/^{171}Yb (for both Yb and Lu isotope ratios) and ^{179}Hf/^{177}Hf (for Hf isotope ratios) of Chu and others (2002). The isobaric interferences of ^{176}Yb and ^{176}Lu on ^{176}Hf were subsequently corrected using the natural abundance ratios of ^{176}Yb/^{173}Yb = 0.79502 and ^{176}Lu/^{175}Lu = 0.02656. Accuracy and external reproducibility of the method were controlled by repeated analyses of reference zircon standards “GJ“ (Morel and others, 2008), “Plešovice” (Sláma and others, 2008), “Mud Tank” and “Temora” (Woodhead and Hergt, 2005), and “QGNG” (Woodhead and others, 2004). The ^{176}Hf/^{177}Hf ratios obtained on all reference materials are within uncertainties identical to the recommended values. Calculations of initial ^{176}Hf/^{177}Hf ratios and ε-Hf were performed applying the ^{176}Lu decay constant of Scherer and others (2001) and ^{176}Hf/^{177}Hf and ^{176}Lu/^{177}Hf values for the chondritic uniform reservoir (CHUR) recommended by Bouvier and others (2008). The quoted uncertainties on initial Hf isotopic composition correspond to the analytical uncertainty and the average 2 S.D (table S6). Reproducibility of the initial Hf isotopic compositions of all measured zircon reference materials (table S7), were propagated by

quadratic addition. More details about the analytical conditions, the data from unknowns, and reference materials are provided in table S7.

RESULTS

Sandstone frame work

The studied Triassic and Jurassic sandstones are mainly classified as feldspathic litharenite and lithic arkose (fig. 4A). Cretaceous sandstones are classified as subarkose and sublitharenite. The Paleocene sandstone sample is a litharenite. Quartz grains of all samples are mostly monocrystalline (~50% in Triassic, 50-75% in Middle Jurassic, and >80% in Cretaceous and Paleocene sandstones; figs. 4A, 4B, 4C and table S2). K-feldspars are dominant in feldspar grains (~73% in the Jurassic, and ~80% in the Cretaceous and Paleocene sandstones; fig. 4B and table S2). From Jurassic to Cretaceous and Paleocene sandstones, the percentage of monocrystalline quartz and K-feldspar grains increases, while the percentage of polycrystalline quartz and plagioclase grains decreases (figs. 4C and 4d). The Triassic sandstone is rich in volcanics (~55%), with less sedimentary and metamorphic lithics (~45%). Jurassic sandstones are composed of sedimentary (~60%), volcanic (~30%), and metamorphic (~10%) rock fragments. In Cretaceous and Paleocene sandstones, sedimentary and metamorphic rock fragments (together >95%) are dominant, while volcanic lithics are less common (<5%). In both Jurassic and Cretaceous sandstones, sedimentary lithic grains mainly comprise siltstone, limestone, and dolomite, whereas metamorphic lithic grains generally consist of low-grade to medium-grade slate, phyllites, and schists. Volcanic lithic grains mainly represent andesite and volcanic glass (figs. 4C, 4D and table S2). Dominantly volcanic lithics (figs. 4C and 4D) and pyroxene minerals (fig. 5) point toward a transitional arc as the source terrane of the Triassic sandstone, whereas Jurassic samples point to a dissected arc and mixed nature of the source terranes (figs. 4E and 4F). Cretaceous and Paleocene sandstones show a recycled orogenic

source based on their rock fragment distributions, indicating mineralogical maturity (figs. 4E and 4F).

Heavy mineral study

Heavy mineral assemblages of sandstones from the Kopet Dagh are characterized as follows: (1) A group of ultra-stable heavy minerals including zircon, tourmaline, and rutile (ZTR), sphene, monazite, and less stable apatite that are typically derived from acidic to intermediate magmatic rocks and recycled siliciclastic sandstones. The amount of ZTR ranges from 22% of total grain count in the Triassic sandstone and reaches up to 53% of total grain count in Jurassic and up to 74.5% in Cretaceous sandstones (Fig. 5). The percentage of apatite grains ranges between 9% in Triassic and 17.5% in Jurassic sandstones (fig. 5 and table S3). (2) A group of meta-stable heavy minerals including pyroxene and amphibole attributed to mafic magmatic source rocks. The amount of pyroxene in Triassic sandstones reaches up to 64% of the total heavy mineral grains, whereas Jurassic and Cretaceous sandstones contain 24% and 1.5% pyroxene, respectively (fig. 5 and table S3). (3) A third group describes meta-stable minerals, including the epidote group, garnet, chloritoid, andalusite, and staurolite, that are common heavy minerals related to medium- to high-grade metamorphic rocks. The percentage of these minerals varies from 1% of total counted grains in Triassic sandstones to 17% of total counted grains in Paleocene sandstones (fig. 5 and table S3). (4) Fourth, Cr-spinel (up to 4% of total grain count; fig. 5 and table S3) indicates mafic-ultramafic rocks as source of detritus.

Detrital zircon U-Pb ages

Laser ablation ICP-MS U-Pb dating on 2478 detrital zircon grains was conducted on one Lower Triassic low-grade meta-sandstone (Qara-Gheitan Formation), five Jurassic turbiditic sandstones (Kashafrud Formation), three Lower Cretaceous fluvial-deltaic sandstones (Shurijeh

315 Formation), and one Paleocene continental sandstone (Pestehleigh Formation; figs. 2, 3, 6, 7 ,8,
316 9, and tables S1 and S4).
317 Late Triassic (217 Ma) and early Paleoproterozoic (2374 Ma) zircons are the youngest and
318 oldest zircons of 232 analysed detrital zircons from the Lower Triassic sandstone (fig. 7; sample
319 KD-08). This sandstone reveals a single probability peak at 337 Ma (early Carboniferous). Five
320 Jurassic sandstones show zircon age distributions between 154 Ma (Late Jurassic) and 2966 Ma
321 (Meso-Archean) based on a total of 1191 dated grains (Fig. 7; samples KD-01, KD-03, KD-06,
322 KD-10, KD-15). Detrital zircons of the Jurassic sandstones are peaking at 232 Ma (Early
323 Triassic), 343 Ma (early Carboniferous), 434 Ma (early Silurian), 643 Ma (middle
324 Neoproterozoic), and 1833 Ma (late Paleoproterozoic; Fig. 7). A total of 865 zircons from three
325 Lower Cretaceous sandstones revealed ages between Early Cretaceous (116 Ma) to
326 Mesoarchean (2861 Ma) (fig. 8; samples KD-02, KD-09, KD-18). The Lower Cretaceous
327 sandstones show a similar zircon age distribution as the Jurassic sandstones, but with an
328 additional zircon probability peak at 132 Ma (Early Cretaceous; fig. 8). The Paleocene
329 sandstone shows ages ranging between 119 Ma (Early Cretaceous) and 2781 Ma (Neoarchean)
330 from 190 dated zircon grains (fig. 8; sample KD-14). The probability peaks of Paleocene
331 sandstone zircon ages are similar to the ones of Cretaceous sandstones (fig. 8). The combined
332 zircon ages call attention to late Paleoproterozoic, middle Neoproterozoic, early Silurian, early
333 Carboniferous, Late Triassic, and Early Cretaceous protoliths in the potential source areas (figs.
334 9 and 10).
335
336 *Hf isotopic composition*
337 Hafnium isotopic composition analysis was conducted on 151 concordantly dated zircon grains
338 with internal growth structures that were large and thick enough to be examined with laser
339 beams. The overall Hf isotopic compositions (epsilon hafnium values: ε-$Hf_{(t)}$) of Triassic to
340 Paleocene sandstones range from -23 to +15 (fig. 11). Late Paleoproterozoic zircon grains

demonstrate evolved ε-$Hf_{(t)}$ values from -13 to +1. Early Silurian zircons show a mixed positive and negative pattern of ε-$Hf_{(t)}$ from -2 to +7 (fig. 11). Early Carboniferous zircons show positive ε-$Hf_{(t)}$ values of -1 to +12 with four grains between -17 and -4 (fig. 11). Similar to early Silurian zircons, the Late Triassic zircons show mixed positive and negative ε-$Hf_{(t)}$ values from -3 to +7 with one outlier of -15. The only analysed Early Cretaceous zircon shows a ε-$Hf_{(t)}$ value of +7.6 (fig. 11).

DISCUSSION

The presented multi-proxy study of Triassic to Palaeocene sandstones from the Kopet Dagh mountains refine our understanding of the corresponding sediment sources and allows for an improved reconstruction of the tectono-sedimentary evolution of the tectonically inverted Kopet Dagh Basin.

Evidence from sandstone frame work

The sandstone modal framework analysis of the sandstone lens within a Triassic polymathic conglomerate (Qara-Gheitan Formation) stipulate a transitional magmatic arc provenance (figs. 4E and 4F). However, petrographic analyses on the Qara-Gheitan sandstones by Ghaemi (2009) specify provenance from a dissected magmatic arc. Additionally, geochemical analysis of large granodiorites and tonalities pebbles of the Qara-Gheitan conglomerate by Zanchetta and others, (2013) suggests an active margin setting with prevailing of I-type plutonic and high-K volcanic rocks. The discrepancy between our results and previously published data can be explained by sampling of different sandstone lenses within the inhomogeneous alluvial Qara-Gheitan Formation.

The mineralogical composition of Middle Jurassic sandstones of the Kashafrud Formation composed of sedimentary and volcanic lithic fragments with subordinate

366 metamorphic lithics (figs. 4C and 4D) suggest a provenance from a dissected
367 magmatic arc and mixed-recycled orogeny (figs. 4E and 4F). Modal framework and
368 paleocurrent analysis along with stratigraphic studies of Middle Jurassic sandstones
369 by Poursoltani and others, (2007) and Poursoltani and Gibling (2011) are in
370 agreement with our results. In addition, they suggested that the detritus was supplied
371 from an active margin in the southeast to the extensional Kopet Dagh Basin in the
372 northwest through channel systems to slope and basin-floor fans forming fluvial
373 (basal conglomerate), deltaic (sandstone), and proximal to distal turbiditic
374 (sandstone and mudstone) facies.
375 Lower Cretaceous sandstones (Shurijeh Formation) show higher mineralogical and
376 textural maturity compared to Middle Jurassic sandstones (figs. 4A, 4B, 4C and 4D)
377 and indicate a recycled orogenic provenance (figs. 4E and 4F). In addition, modal
378 framework analysis by Mortazavi and others (2013) on Lower Cretaceous
379 sandstones supports a provenance characterized by recycled orogenic belts and
380 craton interior signature. Paleocurrent directions of Lower Cretaceous sandstones
381 suggest that sediments were supplied from the south and southwest into the Kopet
382 Dagh Basin (Moussavi-Harami and Brenner, 1990). Therefore, Jurassic sandstones
383 represent a potential source for second-cycle Lower Cretaceous sandstones.
384 Paleocene continental sandstones (Pestehleigh Formation) show relativly higher
385 mineralogical maturity compared to Triassic-Jurassic sandstones (figs. 4A, 4B, 4C
386 and 4D), indicating a recycled orogenic provenance (figs. 4E and 4F). This
387 interpretation agrees with findings of Moussavi-Harami (1993), who suggested that
388 northward and northwestward thinning of coarse-grained Paleocene sandstone layers
389 indicates that the detritus was supplied from the recycling of older sediments in the
390 south and southeast.

Evidence from heavy minerals assemblage

The heavy mineral assemblage of the Triassic sandstone with dominant pyroxene minerals (fig. 5 and table 3) indicates a source from mafic magmatic rocks (probably a magmatic arc), which is in concordance with sandstone modal framework results (figs. 4E and 4F). In addition, the internal textures (CL images) and Th/U ratios of detrital zircons from pebbles of the Triassic conglomerate suggest a magmatic origin for these zircons (Zanchetta and others, 2013). An increase in ultra-stable minerals (ZTR) along with a decreasing percentage of pyroxene minerals in the heavy mineral fraction of Jurassic sandstones (fig. 5 and table 3) imply first-cycle sandstones that were transported over a long distance, or second-cycle sandstone formed by erosion and deposition of pyroclastic-volcanoclastic rocks in a deep-marine basin (Poursoltani and others, 2007). A significant increase of clastic sedimentary lithics compared to the Triassic sandstone and first appearance of garnets in Jurassic sandstones (fig. 5 and table 3) point toward metamorphic rocks as a minor additional source of detritus. Poursoltani and Gibling (2011) reported ultra-stable heavy minerals (ZTR), along with apatite and garnet as the main heavy mineral spectrum in the Jurassic sandstones, coinciding with our findings. Early Cretaceous sandstones indicate a high percentage of ultra-stable minerals (ZTR) and a reduced quantity of pyroxene minerals in the heavy mineral assemblages with a much significant intensity. Vice versa, the amount of pyroxene (20%) in Jurassic sandstones decreases to 1.5% in Cretaceous sandstones (fig. 5 and table 3). This indicates that the heavy mineral content was partly controlled by cannibalism and recycling of older sandstones. An increase of monocrystalline quartz content along with a decrease of less stable volcanic lithics in Early Cretaceous sandstones compared to older lithologies provides further evidence for recycling of Jurassic sandstones (table 3). In addition, based on geochemical analysis of Early Cretaceous sandstones, Mortazavi and others, (2013) suggested moderate to high weathering of the sediments during transportation before deposition, which is in agreement with recycling of older sediments. However, the effect of diagenetic processes on the decrease of metastable

heavy minerals (mostly pyroxene group) and volcanic lithics, and partial alteration of feldspars to clay minerals should not be ignored (Mortazavi and others, 2014; Moussavi-Harami and Brenner, 1993).

Paleocene sandstones indicate a heavy mineral spectrum similar to the one of Early Cretaceous sandstones. However, the amount of garnet increases from 3.5% in Early Cretaceous sandstones to 15.5% in Paleocene sandstones. This implies that erosion of garnet-bearing metamorphic rocks, along with recycling of the older sandstones, were the main sources of detritus in the Palaeocene. The most probable source of garnet and metamorphic lithic grains are Carbo-Permian metamorphic rocks to the southeast of the Kopet Dagh Basin (figs. 2 and 3).

Evidence from Detrital Zircon U-Pb Ages and Hf Isotopes

The 2477 analyzed detrital zircon grains from the Lower Triassic, Middle Jurassic, Lower Cretaceous, and Paleocene turbiditic, deltaic-fluvial, and continental sandstones yielded apparent ages ranging from ca. 119 Ma to ca. 2966 Ma (figs. 7, 8, 9 and 10). Six major U-Pb age groups are identified in the Kopet Dagh detrital zircon.

Mesoarchean to Paleoproterozoic Zircons

The oldest zircons create a broad heterogeneous age spectrum from Mesoarchean to Paleoproterozoic (2966-1600 Ma) with a main peak in the Paleoproterozoic (1833 Ma; fig. 9). Zircons of this population contain ~11% of total dated zircons and are characterized by anhedral to rounded grains without internal zoning (>80%), and a wide range of Th/U ratios (between 0.01 and 2.39; fig. 6 and table S4). The ε-$Hf_{(t)}$ values of Mesoarchean to early Paleoproterozoic zircons represent a mixture of positive and negative values (-6.9 to +10.3), while late Paleoproterozoic zircons show dominantly negative values (-13.6 to -2.3) with only one grain of positive value (+ 1.4; fig. 11 and table S6). Possibly, these are inherited magmatic zircons or fragments of older reworked zircons from crystalline rocks of a craton. Because of the probability of repetitive reworking of detrital zircons through several tectonic cycles since the

443 Archean, the possible metamorphic/igneous source area remains undefined. However, similar
444 age spectra (with a major peak at 2.5 Ga and a minor peak at 1.8 Ga) were reported in
445 Neoproterozoic to Cambrian, lower Permian and Middle Jurassic, and Devonian sandstones of
446 the Alborz mountains (Horton and others, 2008; Moghadam and others, 2017). Also,
447 Mesoarchean to Paleoproterozoic zircons were reported in Cretaceous to Eocene sandstones of
448 Azerbaijan Basin (Mohammadi and others, 2020a), Eocene to Oligocene sandstones from the
449 Sistan Basin (Mohammadi and others, 2016a), and Cretaceous to Miocene sandstones of the
450 Makran Basin in Iran (Mohammadi and others, 2016b; 2017). In addition, similar age spectra
451 were reported in Paleozoic to Triassic sandstones of the Taurides mountains in Turkey (Abbo
452 and others, 2015). There are no reported occurrences of Archean to Paleoproterozoic zircons in
453 the Iranian or Anatolian continental crust (for example Ramezani and Tucker, 2003;
454 Moghadam, and others, 2017; Moghadam, and others, 2020). However, Archean to
455 Paleoproterozoic zircons with main peaks at 2.5 Ga and 1.8 Ga were identified from
456 metamorphic basement of the Afghan block (Faryad and others, 2016), the Tibetan terranes
457 including Songpan Ganzi (Weislogel and others, 2006) and Nan Shan-Qilian Shan-Altun Shan
458 (Gehrels and others, 2011), and the Tarim craton (Gehrels and others, 2011). The lack of a 1.8
459 Ga and presence of a 1.9 Ga zircon age peak in the Archean to Paleoproterozoic age spectrum
460 of Iberia and African Neoproterozoic to Cambrian sandstones (Abdelsalam and others, 2002)
461 excludes the Saharan meta-craton as a potential source area. In fact, the source of Archean to
462 Paleoproterozoic zircons in the Kopet Dagh strata remains enigmatic. Restricting conjecture to
463 the closest cratons points to the nearby Afghan Block with Archean to Paleoproterozoic
464 metamorphic and igneous rocks (Faryad and others, 2016) as an original source area, which
465 supplied detritus to the Kopet Dagh Basin through repetitive recycling of sedimentary
466 successions (fig. 10).

467 *Neoproterozoic Zircons*

468 The second age population includes Neoproterozoic detrital zircons (1000-542 Ma) with a main
469 peak at 643 Ma (fig. 9). This population represents ~18% of the total dated zircons.
470 Neoproterozoic zircons are mostly rounded or anhedral grains with sporadic magmatic or
471 metamorphic growth zoning or lack zoning (fig. 6). Similar to Archean to Paleoproterozoic
472 zircons, Neoproterozoic zircons show Th/U ratios with a wide range between 0.01 and 2.92
473 (table S4), which indicate both magmatic and metamorphic sources. Due to different grain
474 shapes and internal growth structures, Neoproterozoic zircons are probably remnants of older
475 recycled grains or inherited cores from continental crystalline rocks. The ε-$Hf_{(t)}$ values of
476 Neoproterozoic zircons range between -19.3 and +11.3 (fig. 11 and table S6). Neoproterozoic
477 (Pan-African) detrital zircons were reported from several Gondwana-related tectono-
478 stratigraphic domains such as Iran (for example Hassanzadeh and others, 2008; Hosseini and
479 others, 2015; Nutman and others, 2014; Ramezani and Tucker, 2003), the Taurides (Abbo and
480 others, 2015), Libya (Meinhold and others, 2013), the Arabian-Nubian Shield (Morag and
481 others, 2012), and north Africa (Abati and others, 2010; Avigad and others, 2012).
482 Neoproterozoic detrital zircons with a main peak at 559-537 Ma (Cadomian age) were
483 furthermore reported from Alborz and Zagros Neoproterozoic to Paleozoic strata (Horton and
484 others, 2008; Moghadam and others, 2017). In addition, the Neoproterozoic detrital zircons
485 without internal zoning with a main peak at 640-610 Ma were reported from Central Iranian
486 Neoproterozoic to Cambrian sandstones (Honarmand and others, 2016). Nutman and others
487 (2014) reported 637 Ma U-Pb ages of magmatic zircons from the Central Iran crystalline
488 basement (Chadegan orthogneiss). Therefore, repetitive recycling of the Cryogenian to
489 Ediacaran crystalline basement of Central Iran is a plausible source of the Neoproterozoic
490 detrital zircons of Kopet Dagh strata (fig. 10).
491

Ordovician to Silurian Zircons

The third age group denotes Ordovician to Silurian zircons (465-422 Ma) with a peak at 437 Ma with subhedral to euhedral shapes, dominantly magmatic zoning, and Th/U ratios above 0.5 (fig. 6 and table S4), demonstrating an abundant magmatic source. This population contains ~9.3% of the total dated zircons (table S4). ε-$Hf_{(t)}$ values (-1.9 to +6.7, only one grain with -8.9; fig. 11 and table S6) suggest rift-related magmatic rocks as detritus source (for example Vervoort and Blichert-Toft, 1999). Presented zircon ages correspond to major rifting episodes that occurred from late Ordovician to Silurian along the northern Gondwana margins (Moghadam and others, 2020; Ruban, 2007; Stampfli, 2000), which correspond to the separation of the Hun terranes from Gondwana along with the opening of Paleo-Tethys Ocean (Moghadam and others, 2020). Late Ordovician to middle Silurian rift-related magmatism was furthermore reported from northern Central Iran (for example Nowrouzi and others, 2014), eastern Alborz (Derakhshi and Ghasemi, 2015; Moghadam and others, 2020), and Anatolia (for example Topuz and others, 2020; Topuz and others, 2021). In the eastern Alborz, basaltic and basaltic-andesitic magmatism during the Silurian were reported (local name: Soltan Maidan Complex; Derakhshi and Ghasemi, 2015; Ghavidel-Syooki and others, 2011). Geochemistry of this volcanic units shows alkaline affinity with an intra-plate and continental-rift setting (Derakhshi and Ghasemi, 2015). The zircon U-Pb ages of rounded granitic pebbles from conglomerate layers at the base and in middle of the afore-mentioned volcanic unit indicate an early Silurian genesis (434 ± 6.4 Ma; Ghavidel-Syooki and others, 2011). Furthermore, zircon U-Pb ages of A-type granitic pebbles from Devonian sandstones (Padeha Formation) in the eastern Alborz indicate early Silurian ages (441 ± 3.1 Ma) with $\varepsilon Hf_{(t)}$ values ranging from +8.2 to +2.5 (Moghadam and others, 2017). The zircon U-Pb age of granitic pebbles from both Silurian and Devonian successions fit well with the main peak (437 Ma) of the late Ordovician to Silurian detrital zircon population of the Kopet Dagh sandstones (fig. 9). Furthermore, Ordovician to Silurian detrital zircons with a main peak at 435 Ma and $\varepsilon Hf_{(t)}$ values of -3.6 to

+6.3 from late Ordovician (Qelli Formation) sandstones from eastern Alborz were reported by Moghadam and others (2017). Taking into consideration all above-mentioned criteria as well as a short transport distance between eastern Alborz and Kopet Dagh, Ordovician to Silurian detritus of the Kopet Dagh Basin was most probably supplied through recycling of Ordovician to Devonian sandstones from the eastern Alborz.

Devonian to Carboniferous Zircons

The forth age population (385-305 Ma) with a main peak at 340 Ma (fig. 9) exhibits dominantly euhedral zircon grains (~75%) with magmatic internal texture and high Th/U ratios (> 0.5; fig. 6 and table S4). This age spectrum comprises ~17% of the total analysed detrital zircons (table S4). Devonian to Carboniferous zircons display general ε-$Hf_{(t)}$ values between -1.4 and +15.3 and three grains between -12.1 and -17.7 (fig. 11 and table S6). Dominant positive ε-$Hf_{(t)}$ values suggest magmatic zircons with a depleted mantle signature as observed in mafic-ultramafic oceanic crustal and ophiolitic rocks (Patchett, 1983; Blichert-Toft and Albarède, 1997). Carboniferous detrital zircons with a main peak at 344-347 Ma from Cretaceous turbiditic sandstones of Azerbaijan (NW Iran) were reported by Mohammadi and others (2020a). However, a further potential source area includes the northeast of Iran, where Devonian to Carboniferous magmatic rocks were reported from the Aghdarband (Darrehanjir) ophiolite complex (Moghadam and others, 2015a; Zanchetta and others, 2013). The Aghdarband window in the southeast of the Kopet Dagh Basin contains Permo-Triassic undifferentiated sedimentary, low-grade metamorphic, and igneous rocks. Igneous rocks include diabase, gabbro, ultramafic, and volcanoclastic sediments (figs. 2 and 3; Afshar-Harb 1982a; Behrouzi and others, 1993). In the southern part of the Aghdarband complex, an upper Permian to Lower Triassic polymictic conglomerate (Qara-Gheitan Formation; Behrouzi and others, 1993) overthrusts the Triassic unit. The composition and age of the Aghdarband basement is generally poorly constrained. However, the exposed Devonian to Carboniferous meta-sediments in the north of the

544 Aghdarband complex (Behrouzi and others, 1993; Zanchetta and others, 2013) indirectly
545 indicates the basement age of this complex. Besides this, zircon U-Pb ages of plagio-granitic
546 dikes and ferro-diorites (382-380 Ma) from the Darrehanjir ophiolites also indicate a Late
547 Devonian age for this basement complex (Moghadam and others, 2015a). Furthermore, the
548 zircon U-Pb ages of granitoid cobbles in the Qara-Gheitan conglomerate indicate a late
549 Carboniferous (314 Ma) age (Zanchetta and others, 2013). The wide range of Devonian to
550 Carboniferous rocks in the Aghdarband complex is in concordance with detrital zircon ages in
551 the Kopet Dagh sandstones (fig. 9). Supportively, positive zircon $\varepsilon Hf_{(t)}$ values (+13.8 and
552 +14.9) of dated plagio-granites and ferro-diorites suggest a depleted mantel signature
553 (Moghadam and others, 2015a). Devonian and Carboniferous granites and granitioids were
554 reported from the Karakum-Mangyshlak and Karabogaz micro-blocks in Central Asia (for
555 example Natalin and Şengör, 2005). Widespread late Paleozoic to early Mesozoic volcanism in
556 the Turan Block reported by Natalin and Şengör (2005) could represent another possible source
557 for early Carboniferous detrital zircons from the Kopet Dagh. However, the calc-alkaline
558 affinity of these rocks indicates a magmatic arc setting, which is not in agreement with the Hf
559 isotopic composition of detrital zircons. In addition, the reported general SE-NW paleocurrent
560 direction in the Kopet Dagh sandstones (Poursoltani and others, 2007) strengthen the case that
561 the Devonian to Carboniferous detritus was supplied from the Aghdarband Complex rather than
562 from the Turan Block.
563
564 *Permian to Triassic Zircons*
565 The fifth zircon age spectrum in the Kopet Dagh sandstones (300-200 Ma) with a peak at 233
566 Ma (fig. 9) covers ~25.4% of the total dated zircons (table S4). Zircon grains of this population
567 exhibit euhedral shapes (>80%) with magmatic zoning (fig. 6). Furthermore, over 90% of
568 zircons in this spectrum indicate a high Th/U ratio (>0.55; table S4), which denotes magmatic
569 origin. ε-$Hf_{(t)}$ values of Permo-Triassic zircons range between -5.9 and +10.3 (>80%) with two

570 grains with values of -15 and -15.2 (fig. 11 and table S6). Similar to Devonian to Carboniferous
571 zircons, dominant positive ε-$Hf_{(t)}$ values of the Permo-Triassic zircons propose a depleted
572 mantle signature related to mafic-ultramafic rocks from oceanic crust and ophiolite complexes
573 (Patchett, 1983; Blichert-Toft and Albarède, 1997). Both Permian and Triassic ages were
574 reported from the Fariman and Mashhad complexes in the south of the Kopet Dagh Basin (for
575 example Chiu and others, 2017; Ghazi and others, 2001; Karimpour and others, 2010; Kozur
576 and Mostler, 1991; Mirnejad and others, 2013; Moghadam and others, 2015a; Topuz and
577 others, 2018; Zanchetta and others, 2013).
578 The Fariman complex consists of two units: i) The lower metamorphosed unit composed of
579 green schists, metabasites, mafic-ultramafic rocks, and serpentinites, and ii) the upper volcanic-
580 sedimentary unit. Conodonts and radiolarian fossils reveal a late early Permian to middle
581 Permian age for the Fariman complex (Zanchetta and others, 2013). In addition, ^{40}Ar-^{39}Ar
582 dating of magmatic hornblende from olivine cumulates yielded early Permian (276 ±4 Ma) ages
583 for the Fariman complex (Topuz and others, 2018). Furthermore, andesitic dykes dated at 211
584 Ma indicate Late Triassic magmatic activity in the Fariman complex (Zanchetta and others,
585 2013). The Fariman complex has been interpreted as a continental magmatic arc with an intra-
586 arc basin (Zanchetta and others, 2013), a subduction- and plume-related Paleo-Tethyan
587 ophiolite (Moghadam and others, 2015a), as well as a fragment of an oceanic plateau (Topuz
588 and others, 2018).
589 The Mashhad Complex in the south of the Kopet Dagh Basin represents a remnant
590 of the Paleo-Tethys oceanic crust and includes three members: i) The lower member
591 with ultramafics, gabbro-diorites, pillow lavas, marbles, and meta-sediments
592 (Moghadam and others, 2015a). An early Permian age was suggest for the Mashhad
593 ophiolite based on the study of pelagic conodonts (Kozur and Mostler, 1991) and
594 ^{40}Ar-^{39}Ar ages of hornblende from gabbros (287.6 Ma and 281.7; Ghazi and others,
595 2001). ii) The middle member consists of Permo-Triassic deep-water clastic

turbidites and metamorphosed sedimentary rocks (accretionary prism). iii) The upper member exhibits arc-related acidic to intermediate pyroclastic rocks (Moghadam and others, 2015a). Post-collisional intrusive bodies crosscut the Mashhad complex that contain several granitoid and monzogranite suites with zircon U-Pb ages between 200 to 217 Ma (Karimpour and others, 2010; Mirnejad and others, 2013). In addition, the Mashhad granodiorite and Mashhad diorite were dated to 203 Ma and 219 Ma, respectively, with ε-$Hf_{(t)}$ values between -3 to +3 (Chiu and others, 2017). The complex is unconformably is covered by Jurassic terrigenous sediments of the Kashafrud Formation. The southeastward continuation of the Mashhad Complex, which is known as the Torbat-e-Jam Complex, was also intruded by post-collisional I-type granitites (217 Ma; Zanchetta and others, 2013) and gabbro-quartz diorite (215 Ma; Ghavi and others, 2018) of similar ages. According to Zanchetta and others (2013), the age range of post-collisional intrusions indicates that the obduction of the Mashhad ophiolites occurred before the Late Triassic (Norian-Rhaetian).

The age spectrum and dominant positive ε-$Hf_{(t)}$ values of Permian to Triassic zircons, together with the presence of chromium spinel in the heavy mineral assemblage, indicates an exposure of mafic-ultramafic rocks in the source area. This interpretation is in agreement with unroofing and consequent deposition of the Mashhad and Fariman Complexes, and a remnant of Triassic continental arc in the Kopet Dagh Basin. Northward directed paleocurrents and the presence of Norian granodiorite pebbles (211 Ma) in the conglomerate underlying Jurassic sandstones indicate erosion and unroofing of post-collisional intrusive bodies and ophiolitic host rocks in Middle Jurassic time (for example Zanchetta and others, 2013; Zanchi and others, 2009; Zanchi and others, 2016).

Early Cretaceous Zircons

The sixth and youngest age population (146-119 Ma) with a main peak at 132 Ma (fig. 9) contains only 1.5% of the total dated zircon grains (table S4). Zircons grains of this population are euhedral in shape, exhibit magmatic zoning, and show Th/U ratios >0.3 (fig. 6 and table S4). ε-$Hf_{(t)}$ values (+7.6) of this population indicate non-depleted mantle signatures (fig. 11 and table S6). Occurrence of Early Cretaceous zircons in Lower Cretaceous sandstones (samples KD-09 and KD-18) and the Paleocene sandstone (sample KD-14; figs. 8 and 10) indicate syn-sedimentary magmatic activity in the source area. Furthermore, the presence of detrital zircons with early Aptian ages (~124 Ma; average of 8 youngest ages) in Lower Cretaceous sandstones of the Shurijeh Formation indicate maximum depositional ages younger than the previously reported Neocomian stratigraphic age (for example Afshar-Harb 1982a, 1982b; Afshar-Harb and others, 1986; Behrouzi and others, 1993; Mortazavi and others, 2014; Moussavi-Harami and Brenner, 1993). The potential source area of Early Cretaceous zircons could be the Cheste Sharif pluton in north Afghanistan. The Cheste Sharif pluton is located in the Band-e-Bayan Zone (a narrow W-E trending crustal block bounded by the large-scale Hari Rod fault) and is dated at 138 Ma by K-Ar biotite (Debon and others 1987). The presence of Early Cretaceous zircons in Lower Cretaceous sandstones in the eastern Kopt Dagh (fig. 2) is in agreement with a detritus supply from the Band-e-Bayan Zone during Early Cretaceous time. Most probably, Early Cretaceous zircons in the Paleocene sandstones were recycled from Lower Cretaceous sandstones (fig. 10).

REGIONAL TECTONIC IMPLICATIONS

Integrated provenance analysis including zircon ages and isotopic compositions of the Mesozoic to Paleocene detrital material in the Kopet Dagh Basin recorded three main tectonic events in the Phanerozoic (figs. 9 and 11). These events took place in late Ordovician to early Silurian (main peak at 437 Ma), Late Devonian to early Carboniferous (main peak at 340 Ma),

and late Permo-Triassic (main peak at 233 Ma). The first event (late Ordovician to early Silurian) corresponds to the separation of Eurasia from Gondwana and the consequent opening of the Paleo-Tethys Ocean (for example Stampfli and Borel, 2002; Stampfli and others, 2013) (fig. 12; 440 Ma). This rifting event is marked by mafic magmatism along the northern margin of Gondwana (Alborz Mountains; Derakhshi and Ghasemi, 2015). Hf-isotopic composition of Kopet Dagh Ordovician-Early Silurian detrital zircons is in agreement with magmatism in a rifting setting.

The second recorded event in late Devonian to early Carboniferous coincides with a plutonic episode with A-type (intra-continental) magmatism in NW Iran (Azerbaijan area) and the Sanandaj-Sirjan Zone (for example Mohammadi and others, 2020b). In addition, late Devonian to early Carboniferous ages are represented by a series of mafic and ultramafic rocks (ophiolites and oceanic igneous complexes) from Turkey in the west to Tibet to the east (for example Moghadam and others, 2015b). This event records the first stages of Paleo-Tethys subduction beneath the Turan Block that initiated in Late Devonian (~380 Ma) and continued until Late Triassic (Moghadam and others, 2015a) (fig. 12; 380 Ma). According to Zanchetta and others (2013), the exposed Devonian to Carboniferous Aghdarband and Permo-Triassic Fariman complexes in NE Iran formed as a back-arc and an intra-arc basin, respectively, along the southern margin of the Turan Block, and related volcanoclastic rocks were supplied from an active magmatic arc in the south of the Kopet Dagh Basin (fig. 12; 340 Ma). Contrariwise, Moghadam and others (2015a) argued that the Aghdarband and Mashhad ophiolites in NE Iran were part of the Paleo-Tethys oceanic crust, where related volcanoclastic rocks were supplied from an active magmatic arc (Silk Road Arc) in the north of the Kopet Dagh Basin. New zircon data presented in this study with depleted mantle composition and a main peak at 340 Ma support the hypothesis of Zanchetta and others (2013) and point toward intensified rifting and spreading of a back-arc basin ~40 Myr after the initiation of the Paleo-Tethys subduction (fig. 12; 380 Ma).

674 The third event (late Permian to late Triassic) coincides with a continental magmatic arc and
675 the final collision of the Paleo-Tethys (fig. 12; 230 Ma). Rifting of the Iran block from
676 Gondwana in Late Paleozoic forced to northward subduction of the Paleo-Tethys Ocean
677 beneath the Turan (Eurasia) plate, which resulted in the formation of a Permo-Triassic
678 continental magmatic arc. The Mashhad Ophiolite Complex was abducted in early Late Triassic
679 (Carnian-Norian; Moghadam and others, 2015b). Finally, collision between the Iran and Turan
680 plates occurred in Late Triassic (Norian-Rhaetian) and was accompanied by the intrusion of
681 several post collisional plutonic bodies into the magmatic arc and the Mashhad Ophiolite
682 Complex (fig. 12; 230 Ma). Finally, unroofing of the magmatic arc, the Mashhad Ophiolite
683 Complex, and related post-collisional intrusions in Middle Jurassic led to deposition of Middle
684 Jurassic turbiditic sandstones in the Kopet Dagh extensional basin (fig. 12; 165 Ma).
685

686 ## CONCLUSIONS

687 The present study assesses the provenance of detrital sediments in Triassic to Paleocene
688 turbiditic, fluvial-deltaic and continental sandstones of the Kopet Dagh Basin in northeast Iran.
689 Over 2470 detrital zircons U-Pb ages yield a spectrum of variable protoliths from Archean to
690 Early Cretaceous (2966 Ma – 119 Ma) with main peaks in Paleoproterozoic (1883 Ma),
691 Neoproterozoic (643 Ma), early Silurian (437 Ma), early Carboniferous (340 Ma), Late Triassic
692 (233 Ma), and a minor peak in Early Cretaceous (132 Ma). The combined U-Pb ages and Hf
693 isotope data indicate that protolith rocks belonged to an early Silurian intracontinental rift
694 (opening of Paleo-Tethys), an early Carboniferous rifting of a back-arc (Aghdarband Basin),
695 and a Late Triassic collisional to post-collisional (Paleo-Tethys collision) magmatism. Our
696 results highlight the timing of Aghdarband Basin opening 40 Ma after subduction initiation of
697 the Paleo-Tethys. Cr-spinel and heavy mineral assemblages imply additional detritus sourcing
698 from ophiolites (Mashhad and Fariman complexes). Our analytical results furthermore suggest
699 that the majority of Jurassic sedimentary detritus sourced from protoliths in the south of the

Kopet Dagh Basin and deposited in a submarine fan-delta complex. Early Cretaceous detritus was supplied from similar protoliths and furthermore from recycled Jurassic turbiditic sandstones. These sediments were deposited in a fluvial-deltaic complex. The Paleocene continental sediments were mainly supplied from recycling of exposed Jurassic to Early Cretaceous sediments.

ACKNOWLEDGMENTS

The work supported by the Swiss National Science Foundation (grant no. 200021-153124/1). We thank the National Iranian Oil Company for logistic support during field trips.

Supplementary Table Captions

Table S1: Geographical location (degree, minute, second), lithology, local formation name, sedimentary environment, age and characteristics of the analyzed samples of eastern Kopet Dagh sandstones. Analysis key: MFA: modal framework analysis, HM: heavy minerals, DZA: detrital zircon age and Hafnium isotopes.

Table S2: Sandstone framework data and calculated percentages for eastern Kopet Dagh sandstones.

Table S3: Heavy mineral data, calculated percentages and heavy mineral indexes of eastern Kopet Dagh sandstones.

Table S4: Zircon U-Pb isotopic data and calculated ages for eastern Kopet Dagh sandstones. C= Coarse grain (>200µ) and M= Medium grain (100-200µ).

Table S5: Zircon U-Pb dating details including sample preparation, analytical conditions, laser ablation system, ICP-MS instrument, data from unknowns and reference materials, and data processing.

Table S6: Lu-Hf isotopic data and calculated ratios for eastern Kopet Dagh sandstones.

Table S7: Zircon Lu-Hf isotopic analyses details including sample preparation, analytical conditions, laser ablation system, ICP-MS instrument, data from unknowns and reference materials, and data processing.

REFERENCES

Abati J., Aghzer A. M., Gerdes A., Ennih N., 2010, Detrital zircon ages of Neoproterozoic sequences of the Moroccan Anti-Atlas belt: Precambrian Research, v. **181**, n. 1-4, p. 115- 128,

Abbo A., Avigad D., Gerdes A., Güngör T., 2015, Cadomian basement and Paleozoic to Triassic siliciclastics of the Taurides (Karacahisar dome, south-central Turkey): paleogeographic constraints from U–Pb–Hf in zircons: Lithos, v. **227**, p. 122-139,

Abdelsalam M. G., Liégeois J. P., Stern R. J., 2002, The Saharan metacraton: Journal of African Earth Sciences, v. **34**, n. 3-4, p. 119-136,

Afshar-Harb A., Aghanabati A., Shahrabi M., Davoudzadeh M., Madjdi B., Alavi Tehrani N., 1986, Mashhad geological quadrangle map, Connecticut: Geological survey of Iran, scale 1:250,000.

Afshar-Harb A., 1982b, Darreh Gaz geological quadrangle map, Connecticut: National Iranian Oil Company, scale 1:250,000.

Afshar-Harb A., 1982a, Sarakhs geological quadrangle map, Connecticut: National Iranian Oil Company, scale 1:250,000.

Alavi M., 1996, Tectonostratigraphic synthesis and structural style of the Alborz mountain system in northern Iran: Journal of Geodynamics, v. **21**, n. 1, p. 1-33,

Alavi M., Vaziri H., Seyed-Emami K., Lasemi Y., 1997, The Triassic and associated rocks of the Nakhlak and Aghdarband areas in central and northeastern Iran as remnants of the southern Turanian active continental margin: Geological Society of America Bulletin, v. **109**, n. 12, p. 1563-1575,

Allen M. B., Ghassemi M. R., Shahrabi M., Qorashi M., 2003, Accommodation of late Cenozoic oblique shortening in the Alborz range, northern Iran: Journal of Structural Geology, v. **25**, n. 5, p. 659-672,

Avigad D., Gerdes A., Morag N., Bechstädt T., 2012, Coupled U–Pb–Hf of detrital zircons of Cambrian sandstones from Morocco and Sardinia: implications for provenance and Precambrian crustal evolution of North Africa: Gondwana Research, v. **21**, n. 2-3, p. 690-703,

Behrouzi A., Eftekhar Nezhad J., Alavi Naini M., 1993, Torbat-e-Jam geological quadrangle map, Connecticut: Geological survey of Iran, scale 1:250,000.

Barbarin B., 1999, A review of the relationships between granitoid types, their origins and their geodynamic environments: Lithos, v. **46**, n. 3, p. 605-626,

Berberian M., King G. C. P., 1981, Towards a paleogeography and tectonic evolution of Iran: Canadian Journal of Earth Sciences, v. **18**, n. 2, p. 210-265,

Blichert-Toft J., Albarède F., 1997, The Lu-Hf isotope geochemistry of chondrites and the evolution of the mantle-crust system: Earth and Planetary Science Letters, v. **148**, n. 1-2, p. 243-258,

Boulin J., 1988, Hercynian and Eocimmerian events in Afghanistan and adjoining regions: Tectonophysics, v. **148**, n. 3-4, p. 253-278,

Bouvier A., Vervoort J. D., Patchett P. J., 2008, The Lu–Hf and Sm–Nd isotopic composition of CHUR: constraints from unequilibrated chondrites and implications for the bulk composition of terrestrial planets: Earth and Planetary Science Letters, v. **273**, n. 1-2, p. 48-57,

Brown M., 2014, The contribution of metamorphic petrology to understanding lithosphere evolution and geodynamics: Geoscience Frontiers, v. **5**, n. 4, p. 553-569,

Brunet M. F., Cloetingh S., 2003, Integrated peri-Tethyan basins studies (peri-Tethys programme): Sedimentary Geology, v. **156**(1-4), 1- 10.

Brunet M. F., Korotaev M. V., Ershov A. V., Nikishin A. M., 2003, The South Caspian Basin: a review of its evolution from subsidence modelling: Sedimentary geology, v. **156**(1-4), 119-148.

Cawood P. A., Hawkesworth C. J., Dhuime B., 2012, Detrital zircon record and tectonic setting: Geology, v. **40**(10), 875- 878.

Corfu F., Hanchar J. M., Hoskin P. W., Kinny P., 2003, Atlas of zircon textures: Reviews in Mineralogy and Geochemistry, v. **53**(1), 469- 500.

Chiu H. Y., Chung S. L., Zarrinkoub M. H., Melkonyan R., Pang K. N., Lee H. Y., Wang K. L., Mohammadi S. S., Khatib M. M., 2017, Zircon Hf isotopic constraints on magmatic and tectonic evolution in Iran: Implications for crustal growth in the Tethyan orogenic belt: Journal of Asian Earth Sciences, v. **145**, 652- 669.

Chu N. C., Taylor R. N., Chavagnac V., Nesbitt R. W., Boella R. M., Milton J. A., German C. R., Bayon G., Burton K., 2002, Hf isotope ratio analysis using multi-collector inductively coupled plasma mass spectrometry: an evaluation of isobaric interference corrections: Journal of Analytical Atomic Spectrometry, v. **17**(12), 1567- 1574.

Derakhshi M., Ghasemi H., 2015, Soltan Maidan Complex (SMC) in the eastern Alborz structural zone, northern Iran: magmatic evidence for Paleotethys development: Arabian Journal of Geosciences, v. **8**(2), 849- 866.

Dickson J., 1966, Carbonate identification and genesis as revealed by staining: Journal of Sedimentary Research, v. **36**(2), 91- 505.

Dickinson W. R., 1985, Interpreting provenance relations from detrital modes of sandstones, in Zuffa, G.G., ed., Provenance of Arenites: Springer, p. 333–361.

Dickinson W. R., Suczek C. A., 1979, Plate tectonics and sandstone compositions: AAPG Bulletin, v. **63**(12), 2164- 2182.

Debon F., Afzal, H., Le For, P., Sonet J., 1987, Major intrusive stages in Afghanistan: typology, age and geodynamic setting: Geologische Rundschau, v. **76**(1), 245- 264.

Faryad S. W., Collett S., Finger F., Sergeev S. A., Čopjaková R., Siman P., 2016, The Kabul Block (Afghanistan), a segment of the Columbia Supercontinent, with a Neoproterozoic metamorphic overprint: Gondwana Research, v. **34**, 221- 240.

Fedo C. M., Sircombe K. N., Rainbird R. H., 2003, Detrital zircon analysis of the sedimentary record: Reviews in Mineralogy and Geochemistry, v. **53**(1), 277- 303.

Folk R. L., 1980, Petrology of Sedimentary Rocks: Austin, Hemphill Publishing Company, 170 p.

Gehrels G., Kapp P., DeCelles P., Pullen A., Blakey R., Weislogel A., Ding L., Guynn J., Martin A., McQuarrie N., Yin A., 2011, Detrital zircon geochronology of pre-Tertiary strata in the Tibetan-Himalayan orogen: Tectonics, v. **30**, TC5016, doi:10.1029/2011TC002868.

Ghaemi F., 2009, Tectonic setting of sedimentary facies in the Kopet–Dagh Basement: Sedimentary Facies (In Persian), v. 2, n. 1, p. 61- 79.

Ghavi J., Karimpour M. H., Mazaheri S. A., Pan Y., 2018, Triassic I-type granitoids from the Torbat e Jam area, northeastern Iran: Petrogenesis and implications for Paleotethys tectonics: Journal of Asian Earth Sciences, v. **164**, 159- 178.

Ghavidel-Syooki M., Hassanzadeh J., Vecoli M., 2011, Palynology and isotope geochronology of the Upper Ordovician–Silurian successions (Ghelli and Soltan Maidan Formations) in the Khoshyeilagh area, eastern Alborz Range, northern Iran; stratigraphic and palaeogeographic implications: Review of Palaeobotany and Palynology, v. **164**(3-4), 251- 271.

Ghazi A. M., Hassanipak A. A., Tucker P. J., Mobasher K., Duncan R. A., 2001, Geochemistry and 40Ar-39Ar ages of the Mashhad Ophiolite, NE Iran: A Rare Occurrence of a 300 Ma (Paleo-Tethys) Oceanic Crust: In AGU Fall Meeting Abstracts (Vol. 2001, p. V12C-0993).

Gradstein F. M., Ogg G., Schmitz M., 2012, The Geologic Time Scale 2012, Volume Set: Amsterdam, Elsevier, p. 2.

824 Griffin W., Pearson N., Belousova E., Jackson S., Van Achterbergh E., O'Reilly S. Y., Shee S. R., 2000,
825 The Hf isotope composition of cratonic mantle: LAM-MC-ICPMS analysis of zircon
826 megacrysts in kimberlites: Geochimica et Cosmochimica Acta, v. **64**(1), 133- 147.
827 Golonka J., 2004, Plate tectonic evolution of the southern margin of Eurasia in the Mesozoic and
828 Cenozoic: Tectonophysics, v. **381**(1-4), 235-273.
829 Hassanzadeh J., Stockli D. F., Horton B. K., Axen G. J., Stockli L. D., Grove M., Schmitt A. K., Walker
830 J. D., 2008, U-Pb zircon geochronology of late Neoproterozoic–Early Cambrian granitoids in
831 Iran: Implications for paleogeography, magmatism, and exhumation history of Iranian
832 basement: Tectonophysics, v. **451**(1-4), 71- 96.
833 Hellstrom J., Paton C., Woodhead J., Hergt J., 2008, Iolite: Software for spatially resolved LA-(quad
834 and MC) ICP-MS analysis, in Laser ablation ICP-MS in the Earth sciences: Current practices
835 and outstanding issues, P. Sylvester, Editor. 2008, Mineralogical Association of Canada:
836 Vancouver. p. 343-348.
837 Hollingsworth J., Fattahi M., Walker R., Talebian M., Bahroudi A., Bolourchi M. J., Jackson J., Copley
838 A., 2010, Oroclinal bending, distributed thrust and strike-slip faulting, and the accommodation
839 of Arabia–Eurasia convergence in NE Iran since the Oligocene: Geophysical Journal
840 International, v. **181**(3), 1214- 1246.
841 Hollingsworth J., Jackson J., Walker R., Reza Gheitanchi M., Javad Bolourchi M., 2006, Strike-slip
842 faulting, rotation, and along-strike elongation in the Kopeh Dagh Mountains, NE Iran:
843 Geophysical Journal International, v. **166**(3), 1161- 1177.
844 Honarmand M., Li X. H., Nabatian G., Rezaeian M., Etemad-Saeed N., 2016, Neoproterozoic–Early
845 Cambrian tectono-magmatic evolution of the Central Iranian terrane, northern margin of
846 Gondwana: Constraints from detrital zircon U–Pb and Hf–O isotope studies: Gondwana
847 Research, v. **37**, 285- 300.
848 Horstwood M. S., Košler J., Gehrels G., Jackson S. E., McLean N. M., Paton C.,
849
850 Pearson N. J., Sircombe K., Sylvester P., Vermeesch P., Bowring J. F., Condon D. J., Blair Schoene B.,
851 2016, Community-derived standards for LA-ICP-MS U-(Th-) Pb geochronology–Uncertainty
852 propagation, age interpretation and data reporting: Geostandards and Geoanalytical Research,
853 v. **40**(3), 311- 332.
854 Horton B. K., Hassanzadeh J., Stockli D. F., Axen G. J., Gillis R. J., Guest B., Amini A., Fakhari M. D.,
855 Zamanzadeh S. M., Grove M., 2008, Detrital zircon provenance of Neoproterozoic to
856 Cenozoic deposits in Iran: Implications for chronostratigraphy and collisional tectonics:
857 Tectonophysics, v. **451**(1-4), 97- 122.
858 Hosseini S. H., Sadeghian M., Zhai M., & Ghasemi H., 2015, Petrology, geochemistry and zircon U–
859 Pb dating of Band-e-Hezarchah metabasites (NE Iran): An evidence for back-arc magmatism
860 along the northern active margin of Gondwana: Geochemistry, v. **75**(2), 207- 218.
861 Karimpour M. H., Stern C. R., Farmer, G. L., 2010, Zircon U–Pb geochronology, Sr–Nd isotope
862 analyses, and petrogenetic study of the Dehnow diorite and Kuhsangi granodiorite (Paleo-
863 Tethys), NE Iran: Journal of Asian Earth Sciences, v. **37**(4), 384- 393.
864 Kavoosi M. A., Lasemi Y., Sherkati S., & Moussavi-Harami R., 2009, Facies analysis and depositional
865 sequences of the Upper Jurassic Mozduran Formation, a carbonate reservoir in the Kopet Dagh
866 Basin, NE Iran: Journal of Petroleum Geology, v. **32**(3), 235- 259.
867 Kozur H., Mostler H., 1991, Pelagic Permian conodonts from an oceanic sequence at Sang-e-Sefid
868 (Fariman, NE-Iran). Abhandlungen der Geologischen Bundesanstalt in Wien, v. **38**, 101- 110.
869 Lasemi Y., 1995, Platform carbonates of the Upper Jurassic Mozduran formation in the Kopet Dagh
870 Basin, NE Iran-facies, palaeoenvironments and sequences: Sedimentary Geology, v. **99**(3-4),
871 151- 164.

872 Ludwig K. R., 2003, User's Manual for Isoplot 3.00: A Geochronological Toolkit for Microsoft Excel:
873 Berkeley Geochronology Center Special Publication 4, 73 p.
874 Lyberis N., Manby G., 1999, Oblique to orthogonal convergence across the Turan block in the post-
875 Miocene: AAPG Bulletin, v. **83**(7), 1135- 1160.
876 Mahboubi A., Moussavi-Harami R., Mansouri-Daneshvar P., Nadjafi M., Brenner R. L., 2006, Upper
877 Maastrichtian depositional environments and sea-level history of the Kopet-Dagh
878 Intracontinental Basin, Kalat Formation, NE Iran: Facies, v. **52**, 237- 248. doi 10.1007/s10347-
879 005-0034-0
880 Mange M. A., Maurer H. F., 1992, Heavy Minerals in Colour: London, Chapman & Hall, p. 147,
881 doi:10.1007/978-94-011-2308-2.
882 Mangino S., Priestley K., 1998, The crustal structure of the southern Caspian region: Geophysical
883 Journal International, v. **133**(3), 630- 648.
884 Martens J., 1932, Piperine as an immersion medium in sedimentary petrography: The American
885 Mineralogist, v. **17**(5), 198- 199.
886 Meinhold G., Morton A. C., Avigad D., 2013, New insights into peri-Gondwana paleogeography and
887 the Gondwana super-fan system from detrital zircon U–Pb ages: Gondwana Research, v.
888 **23**(2), 661- 665.
889 Mirnejad H., Lalonde A. E., Obeid M., Hassanzadeh J., 2013, Geochemistry and petrogenesis of
890 Mashhad granitoids: An insight into the geodynamic history of the Paleo-Tethys in northeast
891 of Iran: Lithos, v. **170**, 105- 116.
892 Moghadam H. S., Khademi M., Hu Z., Stern R. J., Santos J. F., Wu Y., 2015b, Cadomian (Ediacaran–
893 Cambrian) arc magmatism in the ChahJam–Biarjmand metamorphic complex (Iran):
894 Magmatism along the northern active margin of Gondwana: Gondwana Research, v. **27**(1),
895 439- 452.
896 Moghadam H. S., Li X. H., Ling X. X., Stern R. J., Khedr M. Z., Chiaradia M., Ghorbani G., Arai S.,
897 Tamura A., 2015a, Devonian to Permian evolution of the Paleo-Tethys Ocean: new evidence
898 from U–Pb zircon dating and Sr–Nd–Pb isotopes of the Darrehanjir–Mashhad "ophiolites",
899 NE Iran: Gondwana Research, v. **28**(2), 781- 799.
900 Moghadam H. S., Li Q. L., Griffin W. L., Stern R. J., Ishizuka O., Henry H., and others 2020, Repeated
901 magmatic buildup and deep "hot zones" in continental evolution: The Cadomian crust of Iran:
902 Earth and Planetary Science Letters, v. **531**, 115989.
903 Moghadam H. S., Li X. H., Santos J. F., Stern R. J., Griffin W. L., Ghorbani G., Sarebani N., 2017,
904 Neoproterozoic magmatic flare-up along the N. margin of Gondwana: The Taknar complex,
905 NE Iran: Earth and Planetary Science Letters, v. **474**, 83- 96.
906 Mohammadi A., Burg J. P., Guillong M., 2020a, The Siah Cheshmeh-Khoy-Misho-Tabriz fault (NW
907 Iran) is a cryptic neotethys suture: evidence from detrital zircon geochronology, Hf isotopes,
908 and provenance analysis: International Geology Review,
909 https://doi.org/10.1080/00206814.2020.1845992
910 Mohammadi A., Burg J. P., Guillong M., von Quadt A., 2017, Arc magmatism witnessed by detrital
911 zircon U-Pb geochronology, Hf isotopes and provenance analysis of Late Cretaceous-Miocene
912 sandstones of onshore western Makran (SE Iran): American Journal of Science, v. **317**, n. 8,
913 p. 941- 964.
914 Mohammadi A., Burg J. P., Winkler W., 2016a, Detrital zircon and provenance analysis of Eocene–
915 Oligocene strata in the South Sistan suture zone, southeast Iran: Implications for the tectonic
916 setting: Lithosphere, v. **8**(6), 615- 632.
917 Mohammadi A., Burg J. P., Winkler W., Ruh J., von Quadt A., 2016b, Detrital zircon and provenance
918 analysis of Late Cretaceous-Miocene onshore Iranian Makran strata: Implications for the
919 tectonic setting: Geological Society of America Bulletin, v. **128**(9-10), 1481- 1499.

Mohammadi A., Moazzen M., Lechmann A., Laurent O., 2020b, Zircon U-Pb geochronology and geochemistry of Late Devonian–Carboniferous granitoids in NW Iran: implications for the opening of Paleo-Tethys: International Geology Review, v. **62**(15), 1931- 1948.

Morel M. L. A., Nebel O., Nebel-Jacobsen Y. J., Miller J. S., Vroon P. Z., 2008, Hafnium isotope characterization of the GJ-1 zircon reference material by solution and laser-ablation MC-ICPMS: Chemical Geology, v. **255**(1-2), 231- 235.

Morag N., Avigad D., Gerdes A., Harlavan Y., 2012, 1000–580 Ma crustal evolution in the northern Arabian-Nubian Shield revealed by U–Pb–Hf of detrital zircons from late Neoproterozoic sediments (Elat area, Israel): Precambrian Research, v. **208**, 197- 212.

Mortazavi M., Moussavi-Harami R., Mahboubi A., 2013, Detrital mode and geochemistry of the Shurijeh Formation (Late Jurassic-Early Cretaceous) in the central and western parts of the intracontinental Kopet-Dagh Basin, NE Iran: Implications for provenance, tectonic setting and weathering processes: Acta Geologica Sinica-English Edition, v. **87**(4), 1058- 1080.

Mortazavi M., Moussavi-Harami R., Mahboubi A., & Nadjafi M., 2014, Geochemistry of the Late Jurassic–Early Cretaceous shales (Shurijeh Formation) in the intracontinental Kopet-Dagh Basin, northeastern Iran: implication for provenance, source weathering, and paleoenvironments: Arabian Journal of Geosciences, v. **7**(12), 5353- 5366.

Moussavi-Harami R., 1993, Depositional history and paleogeography of the lower paleocene redbeds in eastern Kopet-Dagh Basin Northeastern Iran: Journal of Science, v. **4**(2), 126- 143.

Moussavi-Harami R., Brenner R. L., 1990, Lower Cretaceous (Neocomian) fluvial deposits in eastern Kopet-Dagh basin, northeastern Iran: Cretaceous Research, v. **11**(2), 163- 174.

Moussavi-Harami R., Brenner R. L., 1993, Diagenesis of non-marine petroleum reservoirs: The Neocomian (Lower Cretaceous) Shurijeh Formation, Kopet-Dagh Basin, NE Iran: Journal of Petroleum Geology, v. **16**(1), 55- 72.

Muttoni G., Mattei M., Balini M., Zanchi A., Gaetani M., Berra F., 2009, The drift history of Iran from the Ordovician to the Triassic: Geological Society, London, Special Publications, v. **312**(1), 7- 29.

Norman M., 1974, Improved techniques for selective staining of feldspar and other minerals using amaranth: U.S. Geological Survey: Journal of Research, v. **2**, 73- 79.

Nowrouzi Z., Moussavi-Harami R., Mahboubi A., Gharaie M. H. M., Ghaemi F., 2014, Petrography and geochemistry of Silurian Niur sandstones, Derenjal Mountains, East Central Iran: implications for tectonic setting, provenance and weathering: Arabian Journal of Geosciences, v. **7**(7), 2793- 2813.

Natalin B. A., Şengör A. C., 2005, Late Palaeozoic to Triassic evolution of the Turan and Scythian platforms: the pre-history of the Palaeo-Tethyan closure: Tectonophysics, v. **404**(3-4), 175-202.

Nutman A. P., Mohajjel M., Bennett V. C., Fergusson C. L., 2014, Gondwanan Eoarchean–Neoproterozoic ancient crustal material in Iran and Turkey: zircon U–Pb–Hf isotopic evidence: Canadian Journal of Earth Sciences, v. **51**(3), 272- 285.

Patchett P. J., 1983, Hafnium isotope results from mid-ocean ridges and Kerguelen: Lithos, v. **16**(1), 47-51.

Paton, C. Woodhead J. D., Hellstrom J. C., Hergt J. M., Greig A., Maas R., 2010, Improved laser ablation U-Pb zircon geochronology through robust downhole fractionation correction: Geochemistry, Geophysics, Geosystems, v. **11**(3), 1- 36.

Petrus J.A., Kamber B. S., 2012, VizualAge: A novel approach to laser ablation ICP-MS U-Pb geochronology data reduction. Geostandards and Geoanalytical Research, v. **36**(3), 247- 270.

967 Pirouz M., Avouac J. P., Hassanzadeh J., Kirschvink J. L., Bahroudi A., 2017, Early Neogene foreland
968 of the Zagros, implications for the initial closure of the Neo-Tethys and kinematics of crustal
969 shortening: Earth and Planetary Science Letters, v. **477**, 168- 182.
970 Poursoltani M. R., Gibling M. R., 2011, Composition, porosity, and reservoir potential of the Middle
971 Jurassic Kashafrud Formation, northeast Iran: Marine and Petroleum Geology, v. **28**(5), 1094-
972 1110.
973 Poursoltani M. R., Moussavi-Harami R., Gibling M. R., 2007, Jurassic deep-water fans in the Neo-
974 Tethys Ocean: the Kashafrud Formation of the Kopet-Dagh basin, Iran: Sedimentary Geology,
975 v. **198**(1-2), 53- 74.
976 Ramezani J., Tucker, R. D., 2003, The Saghand region, central Iran: U-Pb geochronology, petrogenesis
977 and implications for Gondwana tectonics: American Journal of Science, v. **303**(7), 622- 665.
978 Rezaeian M., Carter A., Hovius N., Allen M. B., 2012, Cenozoic exhumation history of the Alborz
979 Mountains, Iran: New constraints from low-temperature chronometry: Tectonics, v. **31**(2),
980 TC2004, doi: 10.1029/2011TC002974.
981 Robert A. M. M., Letouzey J., Kavoosi M. A., Sherkati S., Müller C., Vergés J., 2014,
982 Structural evolution of the Kopeh Dagh fold-and-thrust belt (NE Iran) and
983 interactions with the South Caspian Sea Basin and Amu Darya Basin: Marine and
984 Petroleum Geology, v. **57**, p. 68- 87.
985 Ruban D. A., 2007, Late paleozoic transgressions in the Greater Caucasus (Hun
986 Superterrane, Northern Palaeotethys): Global Eustatic Control. Cadernos do
987 Laboratorio Xeolóxico de Laxe, v. **32**, p. 13- 24
988 Ruh J. B., 2019, Effects of fault-weakening processes on oblique intracontinental rifting and
989 subsequent tectonic inversion. American Journal of Science, v. **319**(4), p. 315- 338.
990 Ruh J. B., Vergés J., 2018, Effects of reactivated extensional basement faults on structural evolution of
991 fold-and-thrust belts: Insights from numerical modelling applied to the Kopet Dagh
992 Mountains: Tectonophysics, v. **746**, 493- 511.
993 Scherer E., Münker C., Mezger K., 2001, Calibration of the lutetium-hafnium clock: Science, v.
994 **293**(5530), 683- 687.
995 Şengör A. M. C., 1990a, Plate tectonics and orogenic research after 25 years: A Tethyan perspective:
996 Earth Science Reviews, v. **27**(1-2), 1- 201.
997 Şengör A. M. C., 1990b, A new model for the late Palaeozoic-Mesozoic tectonic evolution of Iran and
998 implications for Oman. Geological Society, London, Special Publications, v. **49**(1), 797- 831.
999 Şengör A. M. C., 1979, Mid-Mesozoic closure of Permo–Triassic Tethys and its implications: Nature,
1000 v. **279**(14), 590-593.
1001 Şengör A. M. C., Yılmaz Y., Sungurlu O., 1984, Tectonics of the Mediterranean Cimmerides: nature
1002 and evolution of the western termination of Palaeo-Tethys: Geological Society, London,
1003 Special Publications, v. **17**(1), 77- 112.
1004 Sláma J., Košler J., Condon D. J., Crowley J. L., Gerdes A., Hanchar J. M., Horstwood M. S. A., Morris
1005 G. A., Nasdala L., Norberg N., Schaltegger U., Schoene B., Tubrett M. N., Whitehouse M. J.,
1006 2008, Plešovice zircon—a new natural reference material for U–Pb and Hf isotopic
1007 microanalysis: Chemical Geology, v. **249**(1-2), 1- 35.
1008 Stampfli G. M., 2000, Tethyan oceans: Geological society, London, special publications, v. **173**(1), 1-
1009 23.
1010 Stampfli G. M., Borel G. D., 2002, A plate tectonic model for the Paleozoic and Mesozoic
1011 constrained by dynamic plate boundaries and restored synthetic oceanic isochrons:
1012 Earth and Planetary Science Letters, v. **196**(1-2), 17- 33.
1013 Stampfli G. M., Hochard C., Vérard C., Wilhem C., 2013, The formation of Pangea:
1014 Tectonophysics, v. **593**, 1-19.

Stöcklin J., 1974, Possible ancient continental margins in Iran, The geology of continental margins: Springer, New York, 873- 887. doi.org/10.1007/978-3-662-01141-6_64.

Topuz G., Candan O., Okay A. I., von Quadt A., Othman M., Zack T., Wang J., 2020, Silurian anorogenic basic and acidic magmatism in Northwest Turkey: Implications for the opening of the Paleo-Tethys: Lithos, v. **356-357**, 105302.

Topuz G., Candan O., Wang J. M., Li Q. L., Wu F. Y., Yılmaz A., 2021, Silurian A-type metaquartz-syenite to-granite in the Eastern Anatolia: Implications for Late Ordovician-Silurian rifting at the northern margin of Gondwana: Gondwana Research, v. **91**, 1- 17.

Topuz G., Hegner E., Homam S. M., Ackerman L., Pfänder J. A., Karimi H., 2018, Geochemical and geochronological evidence for a Middle Permian oceanic plateau fragment in the Paleo-Tethyan suture zone of NE Iran: Contributions to Mineralogy and Petrology, v. **173**(10), 1- 23.

Thomas J. C., Grasso J. R., Bossu R., Martinod J., Nurtaev B., 1999, Recent deformation in the Turan and South Kazakh platforms, western central Asia, and its relation to Arabia-Asia and India-Asia collisions: Tectonics, v. **18**(2), 201- 214.

Vaezi Pour M. J., Behrouzi A., Alavi Tehrani N., Kholghi M. H., Alavi Naini M., 1992, Torbat-e-Heydarieh geological quadrangle map, Connecticut: Geological survey of Iran, scale 1:250,000.

Vervoort J. D., Blichert-Toft J., 1999, Evolution of the depleted mantle: Hf isotope evidence from juvenile rocks through time: Geochimica et Cosmochimica Acta, v. **63**(3-4), 533- 556.

Weislogel A. L., Graham S. A., Chang E. Z., Wooden J. L., Gehrels G. E., Yang H., 2006, Detrital zircon provenance of the Late Triassic Songpan-Ganzi complex: Sedimentary record of collision of the North and South China blocks: Geology, v. **34**(2), 97- 100.

Weltje G. J., von Eynatten H., 2004, Quantitative provenance analysis of sediments: review and outlook: Sedimentary Geology, v. **171**(1), 1- 11.

Wiedenbeck M. A. P. C., Alle P., Corfu F., Griffin W.L., Meier M., Oberli F.

Von Quadt V., Roddick, J. C., Spiegel W., 1995, Three natural zircon standards for U-Th-Pb, Lu-Hf, trace element and REE analyses: Geostandards Newsletter, v. **19**(1), 1-23.

Wilmsen M., Fürsich F. T., Seyed-Emami K., Majidifard M. R., Taheri J., 2009, The Cimmerian Orogeny in northern Iran: Tectono-stratigraphic evidence from the foreland: Terra Nova, v. **21**(3), 211- 218.

Woodhead J. D., Hergt J. M., 2005, A preliminary appraisal of seven natural zircon reference materials for in situ Hf isotope determination: Geostandards and Geoanalytical Research, v. **29**(2), 183- 195.

Woodhead J., Hergt J., Shelley M., Eggins S., Kemp R., 2004, Zircon Hf-isotope analysis with an excimer laser, depth profiling, ablation of complex geometries, and concomitant age estimation: Chemical Geology, v. **209**(1-2), 121- 135.

Zanchi A., Berra F., Mattei M., Ghassemi M. R., Sabouri J., 2006, Inversion tectonics in central Alborz, Iran: Journal of Structural Geology, v. **28**(11), 2023- 2037.

Zanchi A., Zanchetta S., Berra F., Mattei M., Garzanti E., Molyneux S., Nawab A., Sabouri J., 2009, The Eo-Cimmerian (Late? Triassic) orogeny in North Iran: Geological Society, London, Special Publications, v. **312**(1), 31- 55.

Zanchi A., Zanchetta S., Balini M., Ghassemi M. R., 2016, Oblique convergence during the Cimmerian collision: evidence from the Triassic Aghdarband Basin, NE Iran: Gondwana Research, v. **38**, 149- 170.

Zanchetta S., Berra F., Zanchi A., Bergomi M., Caridroit M., Nicora A., Heidarzadeh, G., 2013, The record of the Late Palaeozoic active margin of the Palaeotethys in NE Iran: constraints on the Cimmerian orogeny: Gondwana Research, v. **24**(3-4), 1237-1266.

Zuffa G. G., 1985, Optical analyses of arenites: Influence of methodology on compositional results, in Zuffa, G.G., ed., Provenance of Arenites: Dordrecht, Holland, Springer, p. 165-189.

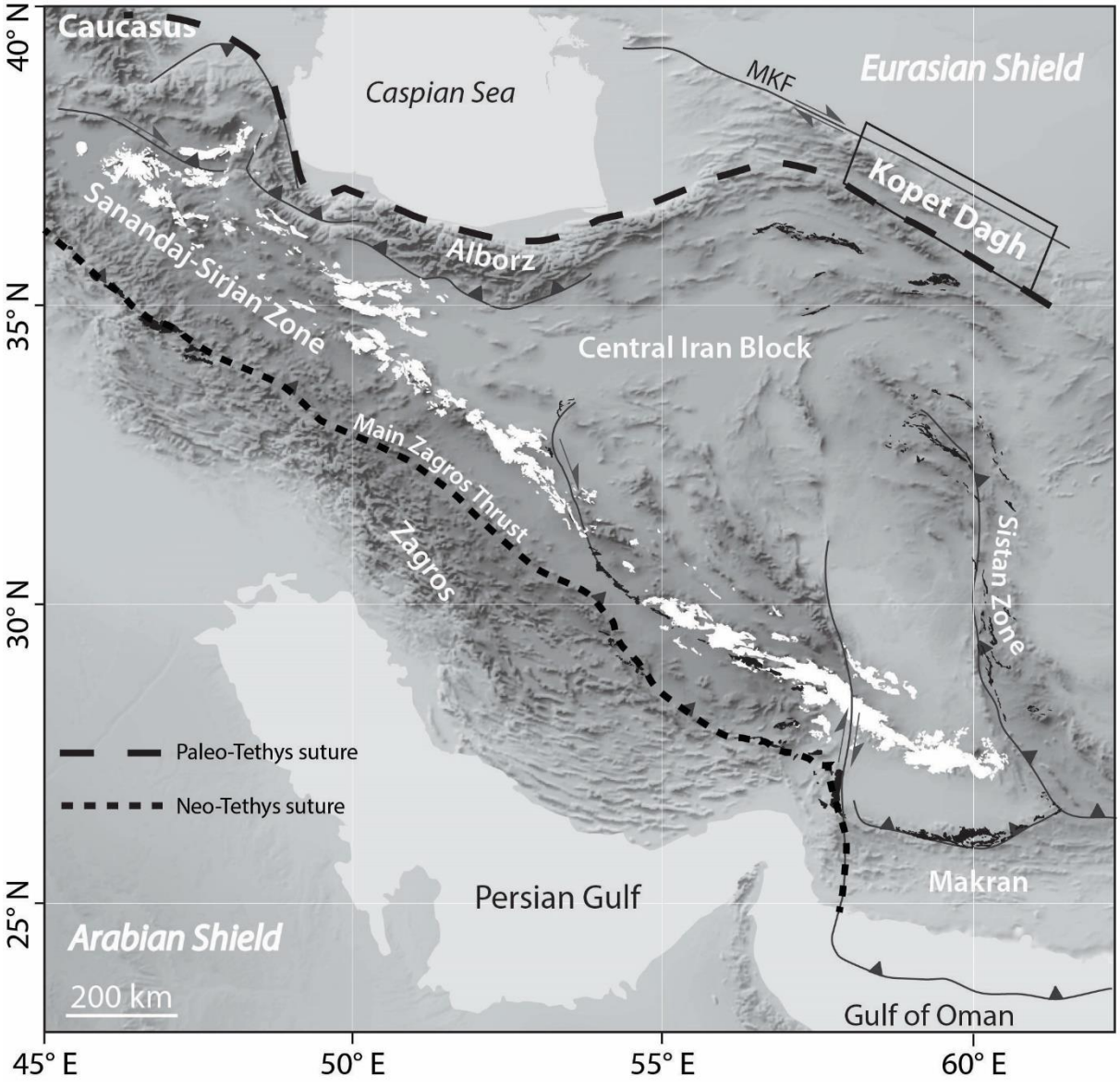

Fig. 1. Simplified tectonic setting of Iran including Urumieh Dokhtar Magmatic Arc (white) and the Tethys ophiolite complexes (black). Framed: eastern Kopet Dagh Basin. Background: shaded relief map ETOPO1 (http://www.ngdc.noaa.gov/mgg/global/relief/ETOPO1).

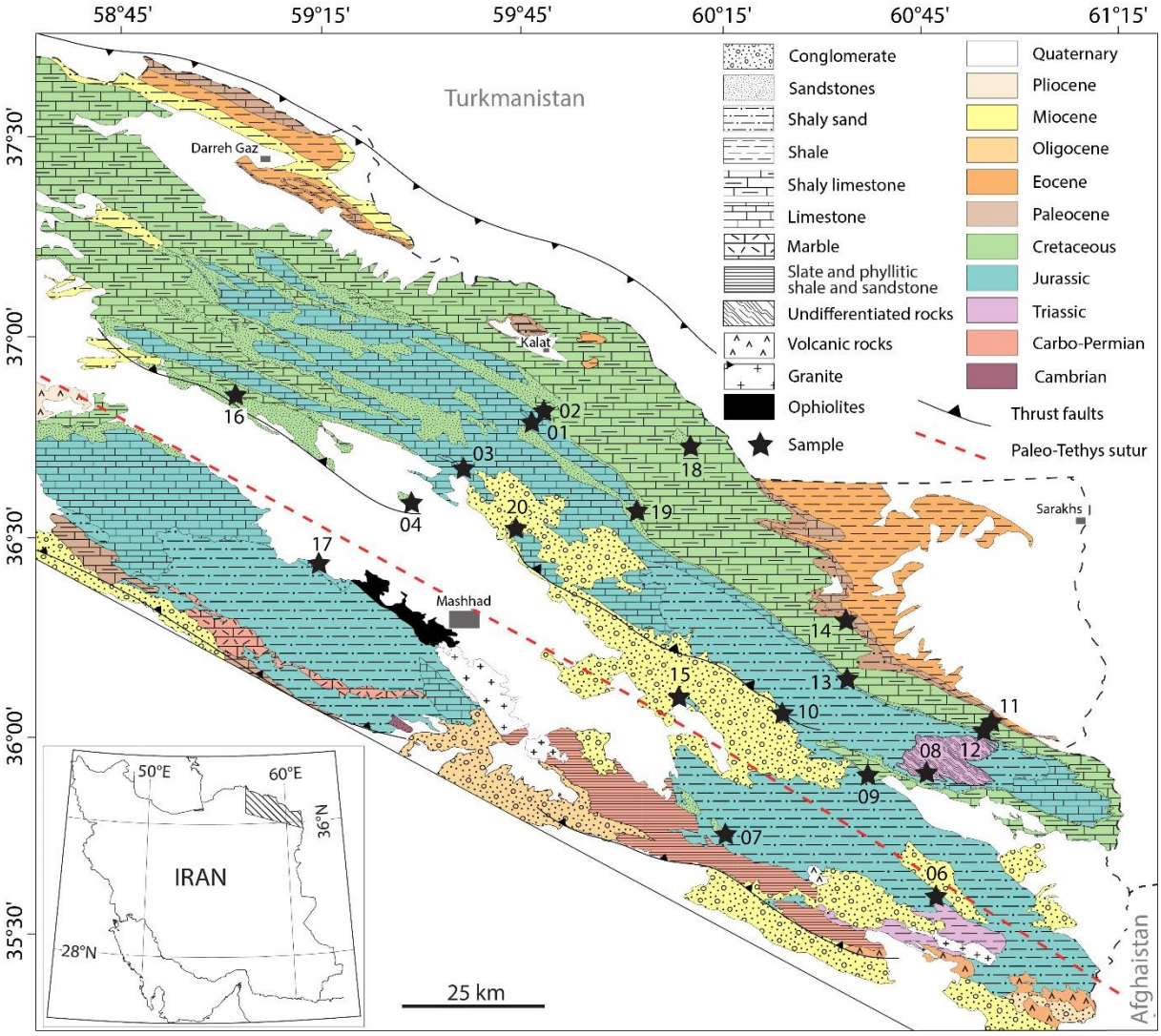

Fig. 2. Simplified geologic map of the East Kopet Dagh Basin and samples location. Stratigraphic ages correspond to the 1:250,000 geological maps of Sarakhs (Afshar-Harb, 1982a), Darreh Gaz (Afshar-Harb, 1982b), Mashhad (Afshar-Harb and others, 1986), and Torbat-e-Jam (Behrouzi and others, 1993).

Fig. 3. Composite stratigraphic section of the East Kopet Dagh Basin with local formation names, sampled formations, and comments on lithology and sedimentary environment. Stratigraphic ages correspond to the 1:250,000 geological maps of Sarakhs (Afshar-Harb, 1982a), Darreh Gaz (Afshar-Harb, 1982b), Mashhad (Afshar-Harb and others, 1986), and Torbat-e-Jam (Behrouzi and others, 1993). Black stars: sampled sedimentary sequences.

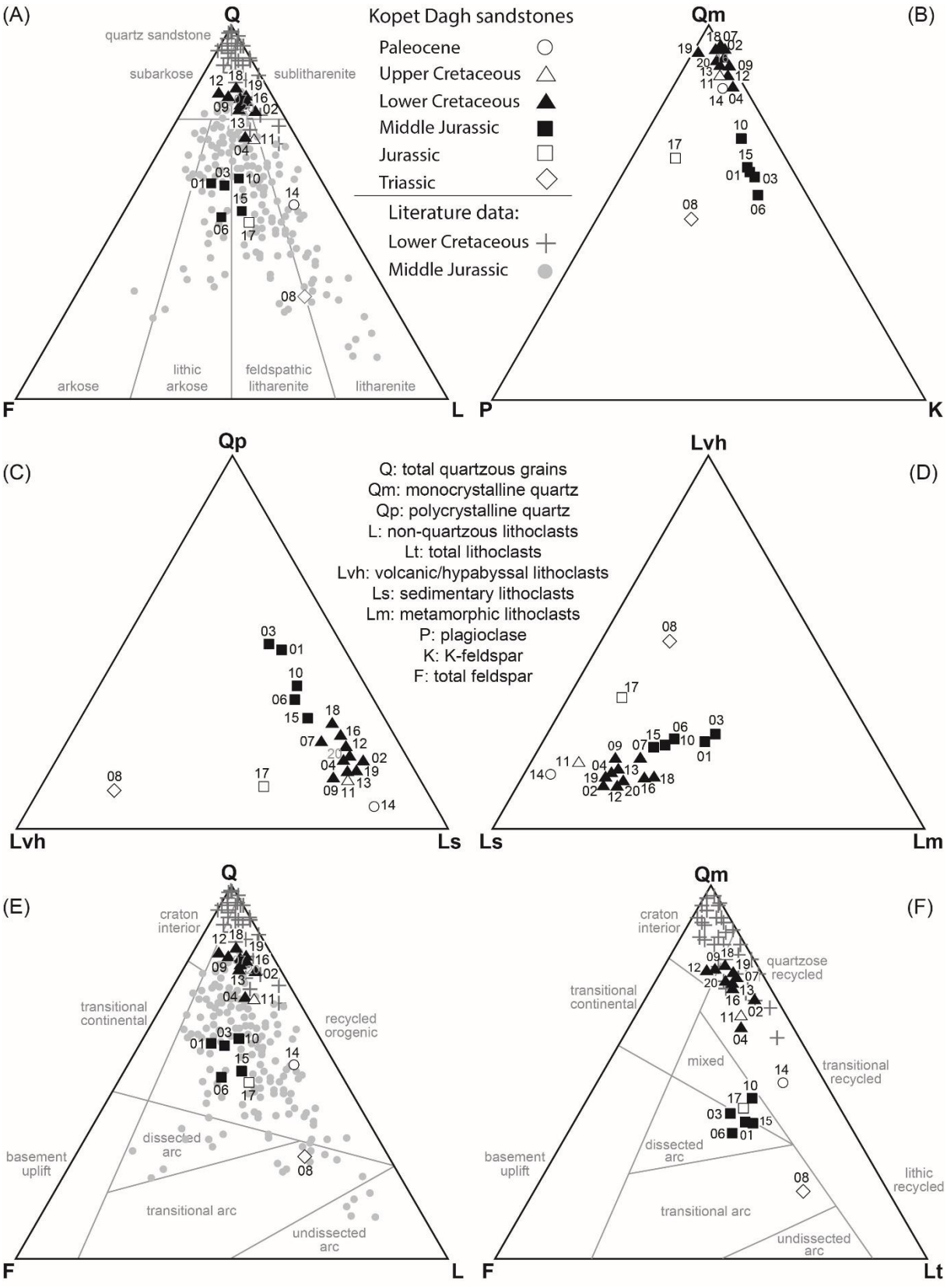

Fig. 4. Detrital composition of Kopet Dagh sandstones in ternary classification schemes and provenance discrimination diagrams. (A) Q-F-L sandstone classification diagram (Folk, 1980); (B) Qm-P-K diagram (after Dickinson and Suczek, 1979); (C) Qp-Lvh-Lsm diagram (after

Dickinson and Suczek, 1979); (D) Lvh-Ls-Lm diagram (after Dickinson, 1985); (E) QFL (Dickinson, 1985); and (F) QmFLt (Dickinson, 1985). Literature data of Middle Jurassic and Lower Cretaceous sandstones from Poursoltani and Gibling (2011) and Mortazavi and others, (2013).

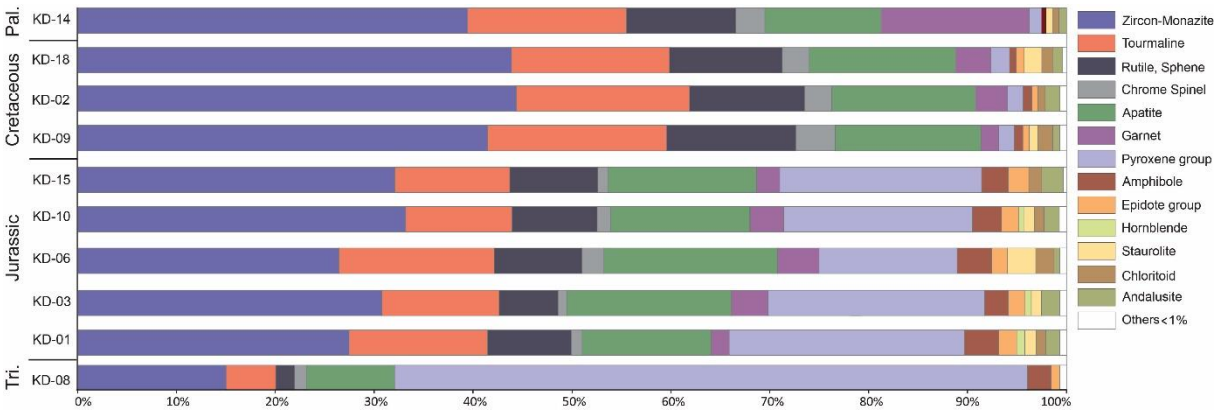

Fig. 5. Heavy mineral assemblages of the Kopet Dagh sandstones arranged by stratigraphic ages displaying the relative abundance of heavy mineral groups.

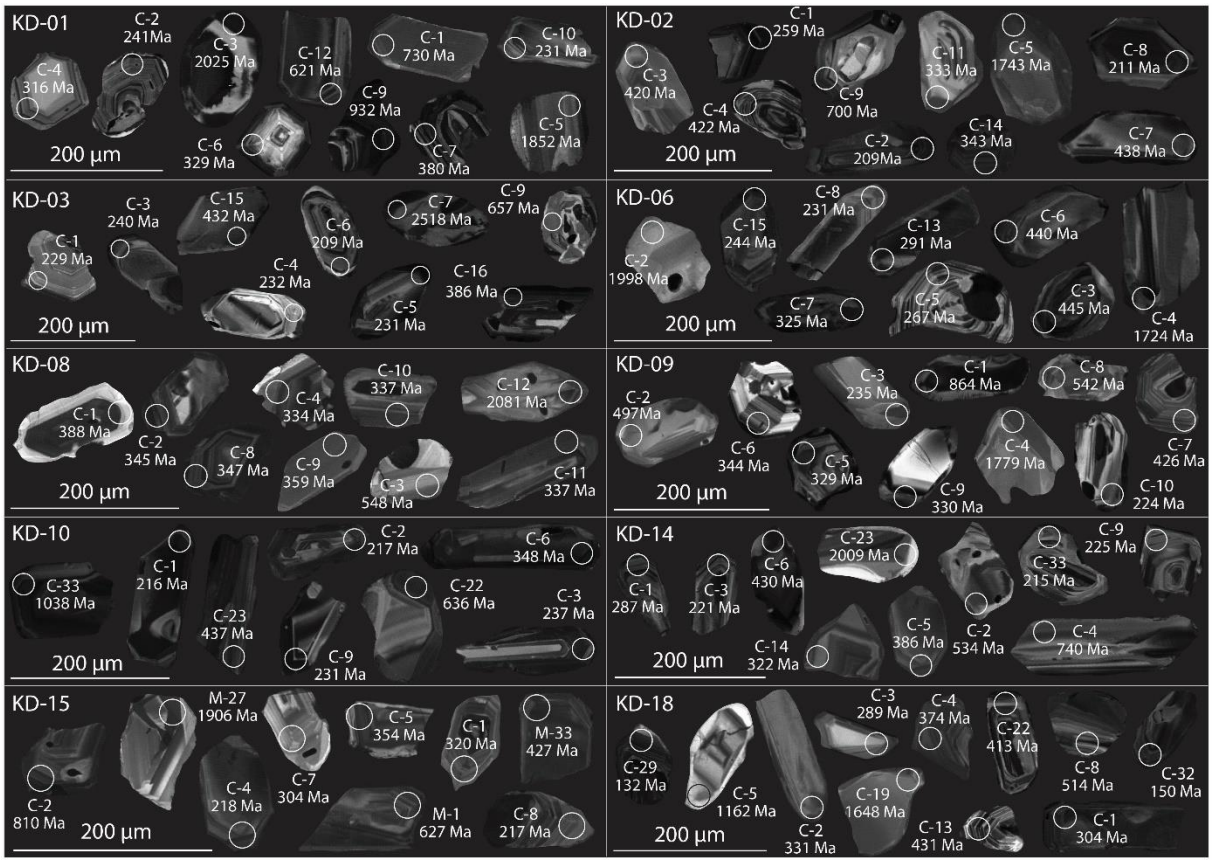

Fig. 6. Representative cathodoluminescence images of dated detrital zircons of the Kopet Dagh sandstones. White circles show laser spot positions for U-Pb age analyses.

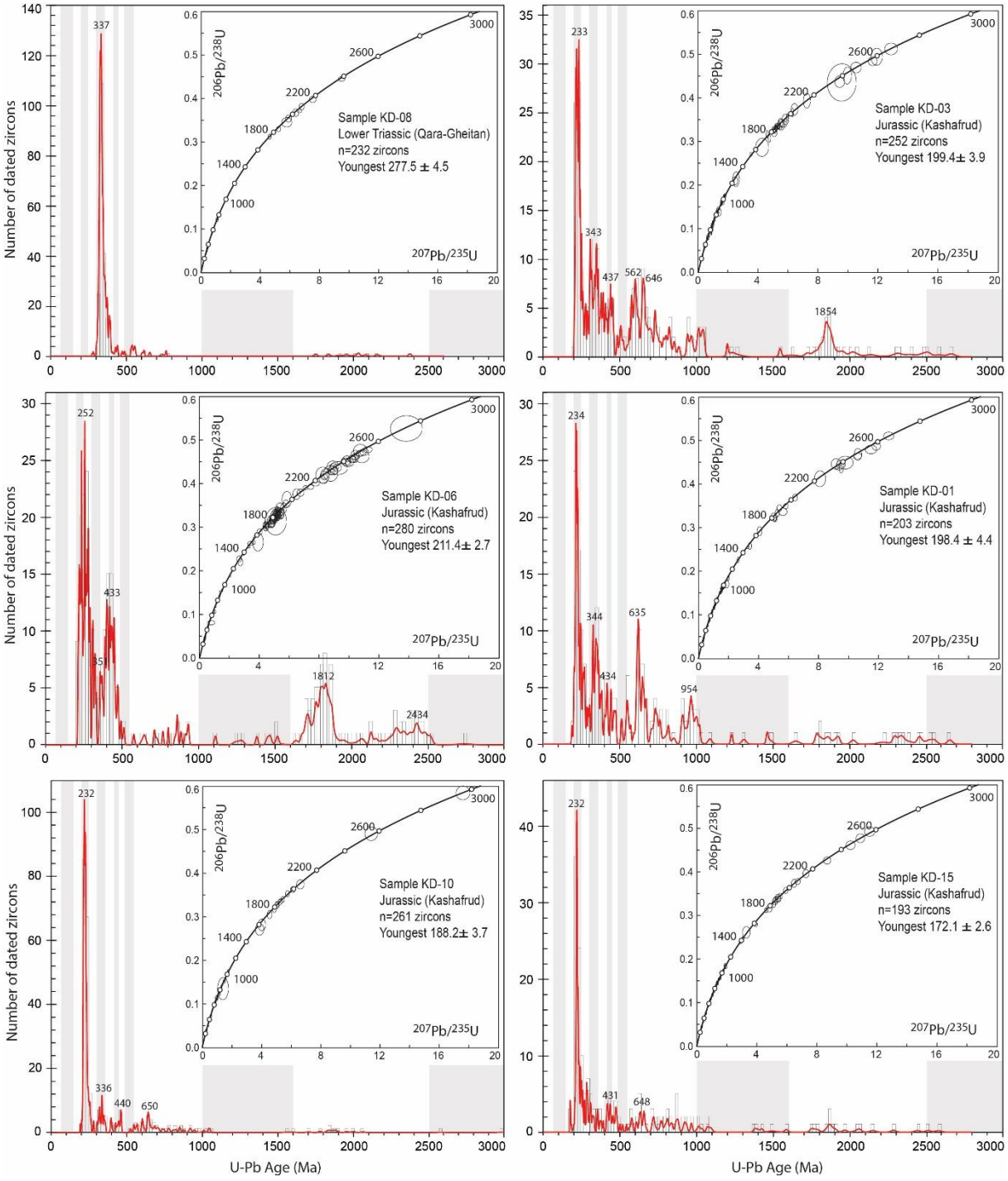

Fig. 7. Detrital zircon $^{206}Pb/^{238}U$ age probability density diagrams with corresponding Concordia plots for the Lower Triassic and Jurassic samples KD-01, KD-03, KD-06, KD-08, KD-10, and KD-15. Ages with discordance greater than 5% are excluded. Time scale after Gradstein and others (2012).

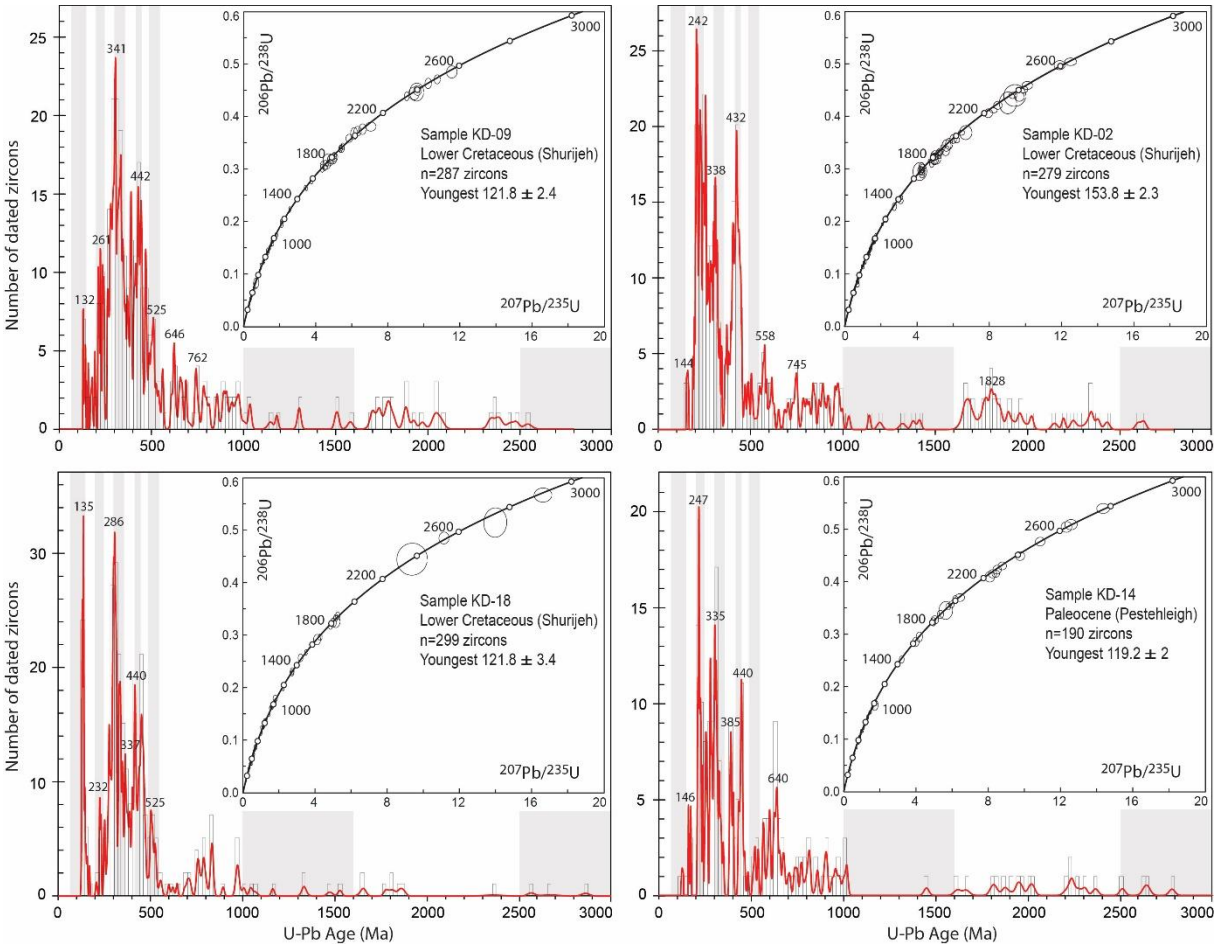

Fig. 8. Detrital zircon $^{206}Pb/^{238}U$ age population probability density diagrams with corresponding Concordia plots for Early Cretaceous and Paleocene samples KD-02, KD-09, KD-14 and KD-18. Ages with discordance greater than 5% are excluded. Time scale after Gradstein and others (2012).

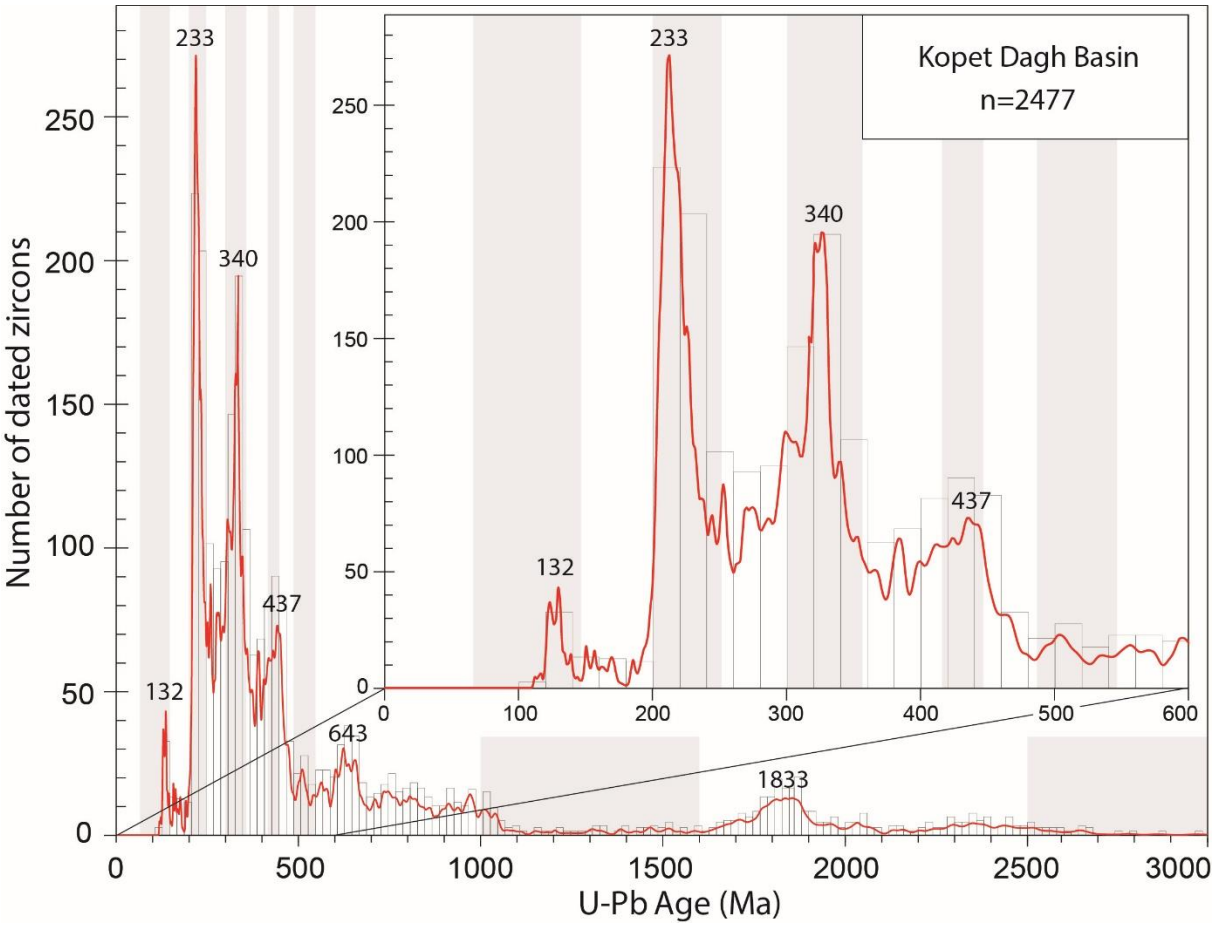

Fig. 9. Combined zircon U-Pb age distribution pattern of Kopet Dagh sandstone samples.

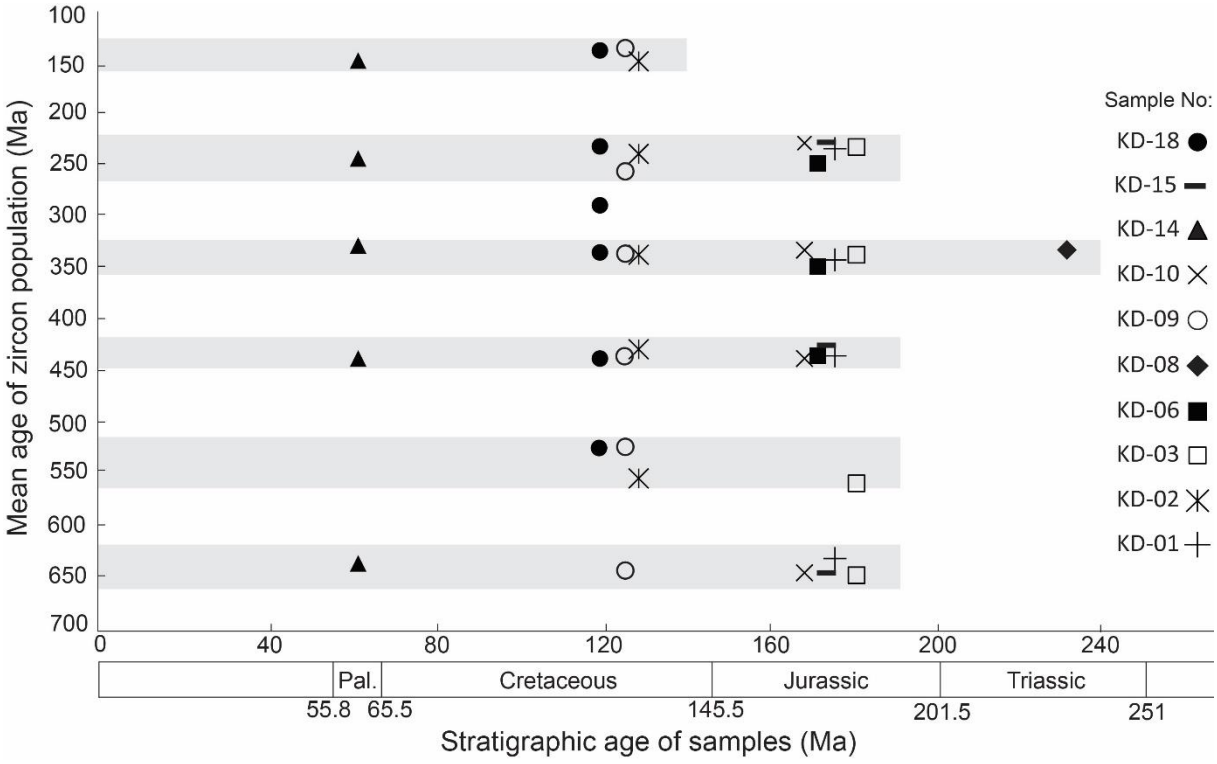

1147

1148 Fig. 10. Detrital zircon U-Pb mean age populations versus stratigraphic age of the Kopet Dagh

1149 sandstones. Time scale after Gradstein and others (2012).

1150

1151

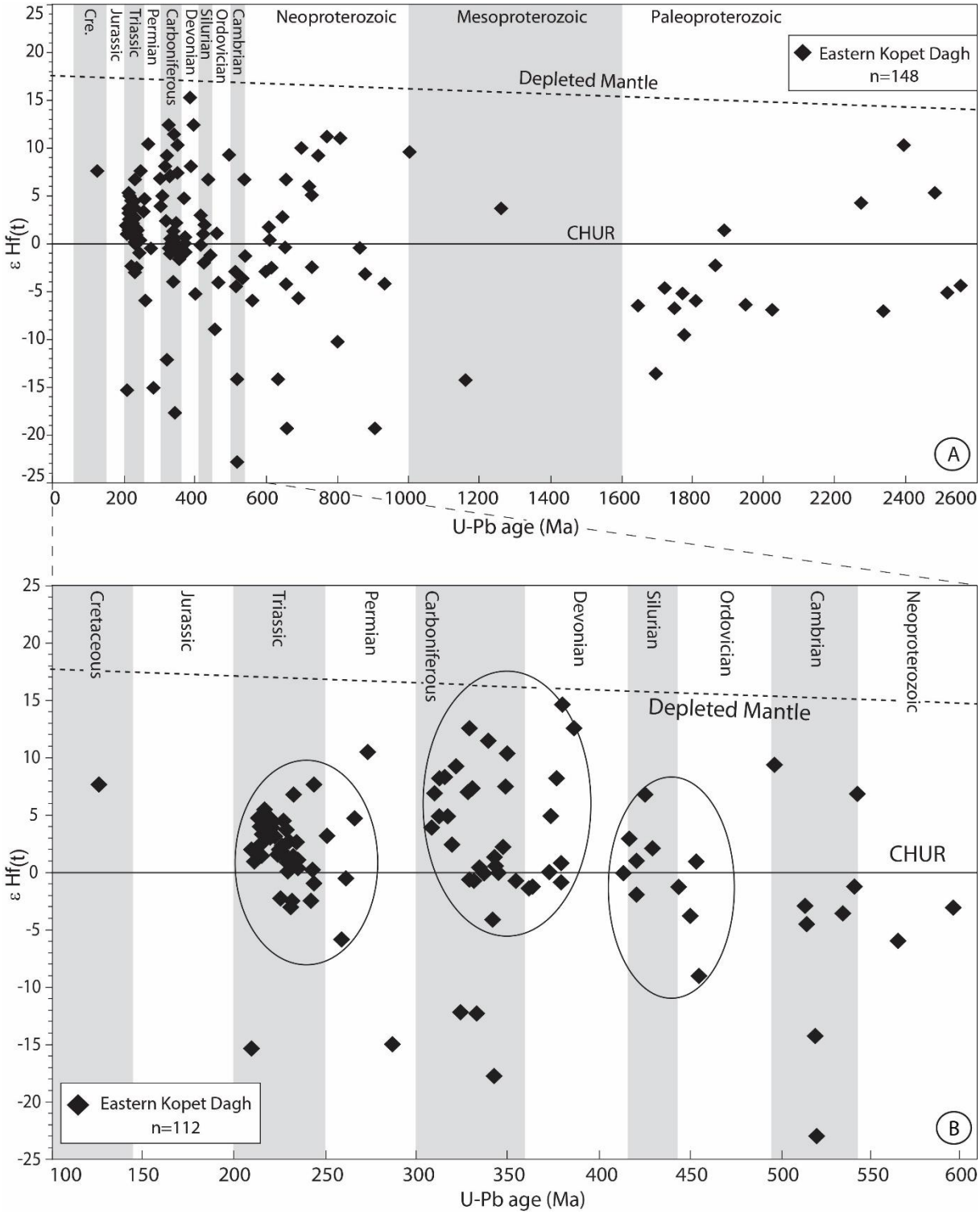

Fig. 11. Time-corrected ε-$Hf_{(t)}$ values versus $^{206}U/^{238}Pb$ ages of Kopet Dagh detrital zircons. Depleted mantle evolution trend (dashed line) from Griffin and others (2000), and Chondritic Uniform Reservoir values (CHUR) from Bouvier and others (2008).

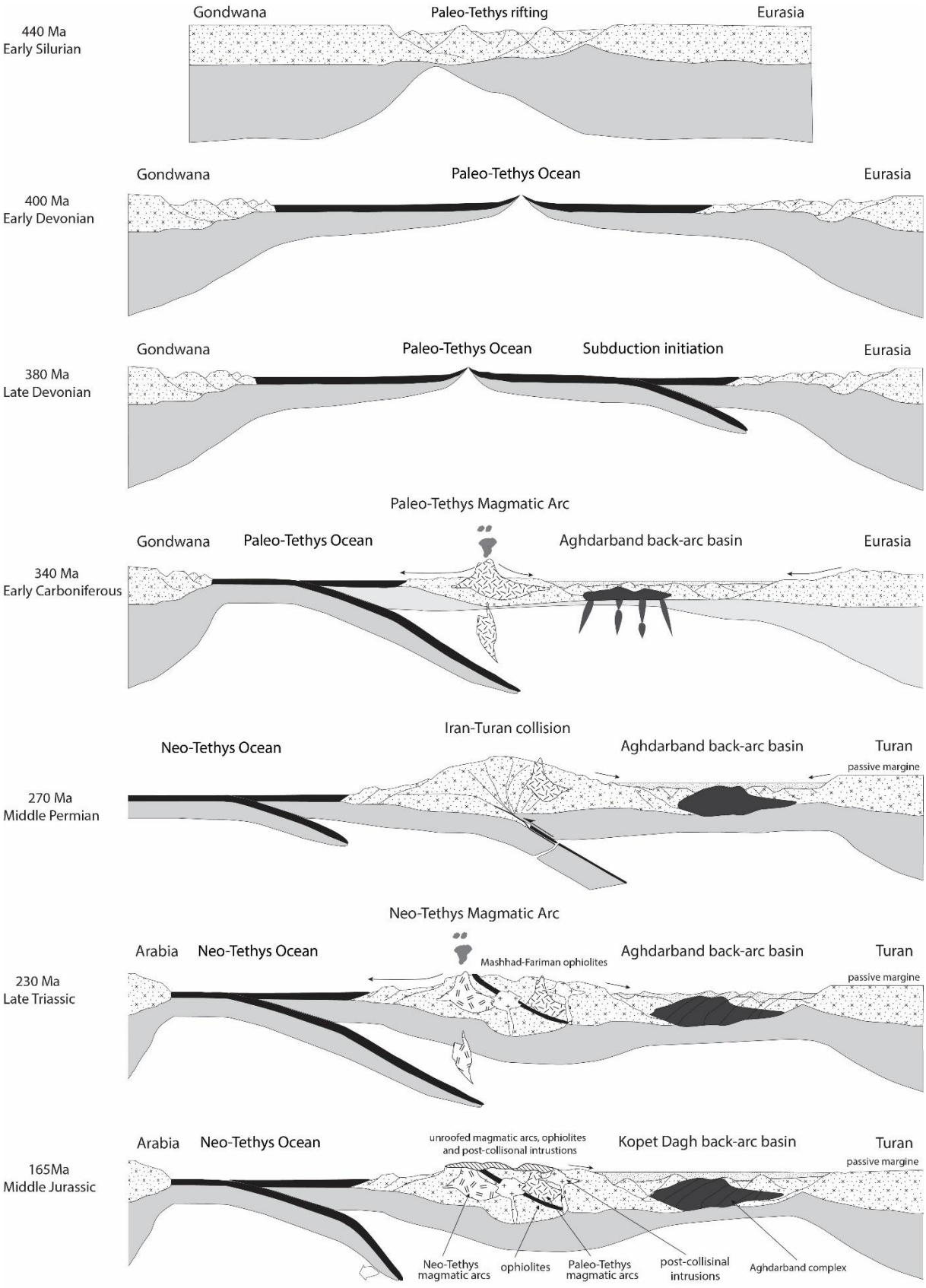

Fig. 12. Tectonic reconstruction along N-S profiles of the Kopet Dagh Basin through time.